

Above- and Belowground Plant Mercury Dynamics in a Salt Marsh Estuary in Massachusetts, USA

Ting Wang¹, Buyun Du^{1,2}, Inke Forbrich^{3,4}, Jun Zhou^{1,5}, Joshua Polen¹, Elsie M. Sunderland⁶, Prentiss H. Balcom⁶, Celia Chen⁷, Daniel Obrist^{1,8*}

¹Department of Environmental, Earth, and Atmospheric Sciences, University of Massachusetts Lowell, Lowell, MA 01854, USA

²College of Environment and Ecology, Jiangsu Open University, Nanjing, 210005, China

³Marine Biological Laboratory, Woods Hole, MA 02543, USA

⁴Department of Environmental Sciences, The University of Toledo, Toledo, OH 43606, USA

⁵Key Laboratory of Soil Environment and Pollution Remediation, Institute of Soil Science, Chinese Academy of Sciences, Nanjing 210008, China

⁶Harvard John A. Paulson School of Engineering and Applied Sciences, Harvard University, Cambridge, MA 02138, USA

⁷Department of Biological Sciences, Dartmouth College, Hanover, NH 03755, USA

⁸Division of Agriculture and Natural Resources, University of California, Davis, CA 95618, USA

Correspondence to: Daniel Obrist (daniel_obrist@uml.edu)

Abstract. Estuaries are a conduit of mercury (Hg) to from watersheds to the coastal ocean, and salt marshes play an important role in coastal Hg cycling. Hg cycling in upland terrestrial ecosystems have been well studied, but processes in densely vegetated salt marsh ecosystems are poorly characterized. We investigated Hg dynamics in vegetation and soils in the Plum Island Sound estuary in Massachusetts, USA, and specifically assessed the role of marsh vegetation for Hg deposition and turnover. Monthly quantitative harvesting of aboveground biomass showed strong linear seasonal increases in Hg associated with plants, with a four-fold increase in Hg concentration and an eight-fold increase in standing Hg mass from June ($3.9 \pm 0.2 \mu\text{g kg}^{-1}$ and $0.7 \pm 0.4 \mu\text{g m}^{-2}$, respectively) to November ($16.2 \pm 2.0 \mu\text{g kg}^{-1}$ and $5.7 \pm 2.1 \mu\text{g m}^{-2}$, respectively). Hg did not increase further in aboveground biomass after plant senescence, indicating physiological controls of vegetation Hg uptake in salt marsh plants. Hg concentrations in live roots and live rhizomes were 11 times and two times higher than concentrations in aboveground live biomass, respectively. Furthermore, live belowground biomass Hg pools (Hg in roots and rhizomes, $108.1 \pm 83.4 \mu\text{g m}^{-2}$) were more than ten times larger than peak standing aboveground Hg pools ($9.0 \pm 3.3 \mu\text{g m}^{-2}$).

A ternary mixing model of measured stable Hg isotopes suggests that Hg sources in marsh aboveground tissues originate from about equal contributions of root uptake (~35%), precipitation uptake (~33%), and atmospheric gaseous elemental mercury (GEM) uptake (~32%). These results suggest a more important role of Hg transport from belowground (i.e., roots) to aboveground tissues in salt marsh vegetation than upland vegetation, where GEM uptake is generally the dominant Hg source. Roots and soils showed similar isotopic signatures suggesting that belowground tissue Hg mostly derived from soil uptake. Annual root turnover results in large internal Hg recycling between soils and plants, estimated at $58.6 \mu\text{g m}^{-2} \text{yr}^{-1}$. An initial mass balance of Hg indicates that the salt marsh presently serves as a small net Hg sink for environmental Hg of $5.2 \mu\text{g m}^{-2} \text{yr}^{-1}$.

1. Introduction

Coastal salt marshes are located at the interface between terrestrial and marine ecosystems and undergo diurnal saltwater inundation by tidal water. They provide important ecological services, have high socioeconomic benefits, and serve as sinks and sources of carbon, nutrients, and contaminants (Hopkinson et al., 2018; Morris et al., 2013). They are at the interface of rivers and oceans,

37 whereby rivers annually transport approximately 27 ± 13 Mmol yr⁻¹ of mercury (Hg) to coastal oceans globally (mostly deposited
38 to estuarine regions (Amos et al., 2014; Liu et al., 2021; Zhang et al., 2015). The location of salt marshes at this interface merits
39 an understanding of their respective Hg sinks and sources and role in coastal Hg cycling. The site of this study was within the Plum
40 Island Sound salt marsh in Massachusetts, USA, the largest macrotidal marsh estuary in New England. The area has been
41 considered a biological mercury (Hg) hotspot, with 62% of saltmarsh sparrows reportedly exceeding a blood Hg threshold that
42 may reduce nesting success (Evers et al., 2007; Jackson et al., 2011; Lane et al., 2020; Lane et al., 2011), although reasons for high
43 Hg exposure are not fully understood. A potentially important Hg source in marshes includes Hg uptake by plants. In terrestrial
44 environments, plants assimilate substantial amounts of atmospheric Hg, which is subsequently transferred to soils via tissue
45 senescence (e.g., litterfall) and wash-off (i.e., throughfall deposition) (Fisher and Wolfe, 2012; Iverfeldt, 1991; Rea et al., 1996;
46 Zhou et al., 2021). This plant Hg uptake is considered dominated by assimilation of atmospheric gaseous elemental Hg (GEM), so
47 that global vegetation acts as a large atmospheric GEM pump to soils (Fu et al., 2019; Jiskra et al., 2018; Obrist et al., 2018; Wang
48 et al., 2019, 2022; Zhou et al., 2021; Zhou and Obrist, 2021). In terrestrial ecosystems, Hg inputs derived from plants are the
49 dominant Hg sources accounting for 60% to 90% of the total Hg inputs to soils (Zhou and Obrist, 2021). Salt marshes are
50 characterized by high plant net primary productivity (NPP) driven by vascular macrophytes, with plant NPP as high and even
51 exceeding that of terrestrial ecosystems (Marques et al., 2011; Tobias and Neubauer, 2009; Visser et al., 2018). For example, salt
52 marsh biomass production across Atlantic and Gulf sites in the U.S. ranges from 228 to 1,335 g C m⁻² yr⁻¹ with a median value of
53 537 g C m⁻² yr⁻¹ (Tobias and Neubauer, 2009). By comparison, NPP across 18 productive U.S. forests ranging between 400 to
54 1,000 g C m⁻² yr⁻¹ (He et al., 2012). As salt marshes are considered strong sinks of atmospheric carbon driven by plant CO₂
55 assimilation (Forbrich et al., 2018), their high NPP also may lead to increased deposition of atmospheric Hg due to vegetation
56 assimilation of atmospheric Hg and subsequent transfer to salt marsh ecosystems via litterfall and plant senescence.
57 We hypothesized that salt marsh plants in the Plum Island estuary salt marsh act as substantial sinks of atmospheric Hg via
58 vegetative assimilation of GEM, and aimed to quantify Hg sources in salt marsh vegetation, accumulation rates, and turnover rates
59 of Hg in salt marsh plants. We quantified Hg fluxes and pools associated with plant dynamics in the salt marsh and Hg associated
60 with annual growth of aboveground tissues, estimated transfer of Hg associated with aboveground tissues to soils, and assessed
61 Hg turnover in belowground biomass. In addition, we quantified specific sources of Hg in salt marsh biomass tissues using stable
62 Hg isotope signatures, with isotope endmembers representing different sources such as plant uptake of atmospheric elemental, root
63 uptake of soil Hg, and precipitation-derived deposition whereby precipitation Hg may include direct deposition to leaves or uptake
64 from soil water (Jiskra et al., 2018; Niu et al., 2011; Zheng et al., 2016).

65 **2. Methods**

66 **2.1. Site Description**

67 Sampling sites were located in the Plum Island Sound on the northeastern coast of Massachusetts, USA (42°45'10", 70°56'46")
68 between the Gulf of Maine and the city of Boston. The estuary is the largest marsh-dominated estuary in New England with a total
69 marsh area of 60 km² and salt marsh area of 40 km² (Hopkinson et al., 2018; Millette et al., 2010). Tides are semidiurnal with an
70 amplitude averaging 2.7 m (NOAA Tide Predictions, 2020). We focused our study on high marsh platforms, with an approximate
71 elevation of 1.4 m above the North American Vertical Datum 88, which dominate tidal marshes in New England and accounts for
72 75% of the vegetated area in the Plum Island Sound estuary (Millette et al., 2010; Wilson et al., 2014). The high marsh exhibits
73 poor water drainage (Wilson et al., 2014) and is generally inundated biweekly during spring tides and during major storms (Millette
74 et al., 2010). The two dominant species on the high marsh are C4 species including *Sporobolus pumilus* (common name: marsh

75 hay) and *Sporobolus alterniflorus* (common name: smooth cordgrass), with the latter mainly distributed along tidal channels and
76 also dominant in low marsh platforms (Anjum et al., 2012; Cheng et al., 2006; Curtis et al., 1990; Maricle et al., 2009; Sun et al.,
77 2020). Another C4 species, *Distichlis spicata* (coastal saltgrass), is often collocated within *S. pumilus* -dominated sites on high
78 marsh platforms (Arp et al., 1993), whereas *Juncus gerardii* (saltmarsh rush) usually dominates the terrestrial boundary of the high
79 marsh (Bertness, 1991).

80 Although the upland watershed of this salt marsh does not have any known point sources of Hg, previous studies pointed to the
81 possibility of legacy anthropogenic sources present in this marsh estuary, possibly from ocean water import of Hg from nearby
82 riverine sources, and other possible sources include regional atmospheric deposition directly to the marsh and its watershed (Evers
83 et al., 2007; Lane et al., 2020; Lane et al., 2011; Wang and Obrist, 2022). A previous of our group showed high Hg concentrations
84 observed in marsh soils and evidence that the salt marsh soils currently serve as a source of Hg to tidal water and the nearby ocean
85 dominated lateral particulate-bound Hg transport (Wang and Obrist, 2022). However, a comprehensive mass balance of Hg inputs
86 and outputs in this system is currently missing.

87 **2.2. Sampling and Processing of Vegetation and Soil**

88 Aboveground biomass of the dominant species, *S. alterniflorus* and *S. pumilus*, were collected every four to five weeks between
89 June and November in 2021, corresponding to the active growing season. Additional senesced biomass was sampled in the
90 following year in April 2022, and two additional salt marsh species, *D. spicata* and *J. gerardii*, were sampled in September 2018.
91 For each sampling date, eight 1-m² square plots were selected in the footprint area of a micrometeorological flux tower (Forbrich
92 et al., 2018), of which four squares were dominated by *S. alterniflorus* and four adjacent squares were dominated by *S. pumilus*.
93 During vegetation sampling, all aboveground vegetation within the 1-m² squares was clipped close to the ground and stored in
94 plastic Ziploc bags in coolers over ice and subsequently in refrigerators until processing. In the laboratory, wet and dry vegetation
95 mass was determined, and vegetation was carefully separated into live and senesced tissues. Note that in these ecosystems,
96 significant amounts of senesced standing tissues from the previous year are present along with current year green tissues. We then
97 prepared the samples for analysis of Hg in both bulk samples and in individual species.

98 In four of the eight sampling sites, quantitative belowground sampling was performed in July 2021, with two plots dominated by
99 *S. alterniflorus* and the other two plots dominated by *S. pumilus*. Soil cores with diameter of 10 cm to a depth of 40 cm were taken
100 and separated into depth increments of 0-20 cm and 20-40 cm. Belowground components were separated into the following
101 components by washing onto a fine mesh with pore size of 0.25 mm: live roots and rhizomes identified by turgidity and color (e.g.,
102 hard and white tissues versus soft and grey/discolored); senesced roots, rhizomes, and soil detritus (not recognizable organic matter);
103 and sediments and fine organic matter that passed through the fine mesh (only analyzed in two subsamples). This process was
104 based on visual separation of tissues (Elsley-Quirk et al., 2011; Valiela et al., 1976). We observed live roots and rhizomes only in
105 the top 20 cm of the soils with no recognizable live roots and rhizomes at 20-40 cm depth. All plant tissues were rinsed with tap
106 water until the water was clean, then thoroughly rinsed three times with Milli-Q water, while a selected number of live aboveground
107 tissues were analyzed both washed and unwashed for estimation of washable Hg (see section of throughfall estimation). All samples
108 were dried at 65 °C to reach a constant weight and were milled and homogenized using stainless steel coffee grinders (for vegetation
109 samples) and 8530 Shatter-Box (for soil samples) prior to analyses. The coffee grinders and Shatter-Box were rinsed with Milli-Q
110 water and dried with Kimwipes between samples.

111 2.3. Hg concentration and stable isotope analysis of vegetation and soils samples

112 Total Hg concentrations in all components were measured using a tri-cell Milestone DMA-80 Direct Mercury Analyzer (Milestone
113 Inc., Monroe, Connecticut, USA) through thermal decomposition, catalytic reduction, amalgamation, desorption, and atomic
114 absorption spectroscopy following EPA method 7473 (U.S. EPA., 1998). The system was re-calibrated based on daily performance
115 checks using five-point calibration curves. Standard reference materials, including NIST 1515 Apple leaves (43.2 $\mu\text{g kg}^{-1}$) and
116 Canadian National Research Council certified reference material MESS-4 (marine sediment, 91 $\mu\text{g kg}^{-1}$), were used as continuous
117 calibration verifications after every ten-samples. Percent recoveries of total Hg for certified reference materials averaged of 99.9
118 \pm 5.5% (range of 89.6% to 111.4%) and all blanks were below detection limits (0.001 ng). All samples were analyzed in triplicate
119 and results were accepted when coefficients of variation were less than 10%.

120 Hg stable isotopes were measured on select samples including live aboveground biomass, live root, live rhizomes, and surface (0-
121 22.5 cm) and deeper soils (97.5 cm). Samples were pre-concentrated with a Nippon direct Hg analyzer (Nippon Instruments) as
122 described in Enrico et al. (2021). A HGX-200 cold vapor generator (Teledyne Cetac Technologies) was used to introduce sample
123 Hg to a Thermo Neptune plus MC-ICP-MS at Harvard University. An Apex-Q nebulizer (Elemental Scientific) was used to
124 nebulize a Thallium (Tl) solution and inject Tl aerosols in the HGX-200. NIST3133 (primary standard) and RM8610 (previously
125 UM- Almaden, secondary standard) were used as Hg isotopic standard solutions, and NIST997 (thallium isotopic standard solution)
126 was used as the reference material to correct instrument mass bias. NIST 1515 Apple leaves and Canadian National Research
127 Council certified reference material MESS-4 were used to verify isotope analysis, and standard recoveries were in the acceptable
128 range (from 82% to 93%). For analysis on Neptune, all trapped samples and standards were diluted with trapping solution to either
129 1 or 2 ng mL⁻¹, which concentrations could be matched with NIST 3133 bracketing standard and the UM-Almaden concentrations.
130 Quality control results for MESS-4 and RM8610 were similar to previously published findings (Table S4, Blum and Johnson, 2017;
131 Enrico et al., 2021). Small delta (δ) annotation is used for mass-dependent fractionation (MDF), which is reported as per mil (‰)
132 values relative to NIST-3133 based on equation (1),

$$133 \delta^{xxx}\text{Hg} = \left(\frac{(^{xxx}\text{Hg}/^{198}\text{Hg})_{\text{sample}}}{(^{xxx}\text{Hg}/^{198}\text{Hg})_{\text{NIST3133}}} - 1 \right) \times 1000 \quad (1)$$

134 where ^{xxx}Hg is the mass of each Hg isotope between 199 and 204. Capital delta (Δ) annotation is used for mass-independent
135 fractionation (MIF), describing fractionation away from the expected MDF based on equation (2),

$$136 \Delta^{xxx}\text{Hg} = \delta^{xxx}\text{Hg} - \beta_{xxx} \times \delta^{202}\text{Hg} \quad (2)$$

137 where ^{xxx}Hg denotes mass of each Hg isotope 199, 200, 201, and 204, and β_{xxx} is the constant mass-dependent correction factor
138 (0.252, 0.502, 0.752, and 1.492, respectively; Blum and Bergquist, 2007). To determine Hg sources, a ternary isotope mixing
139 model was used to estimate fractions of Hg in above-ground biomass. End-member Hg sources used included signatures of salt
140 marsh plants roots measured in this study, published signatures of upland foliage samples as a proxy for atmospheric GEM uptake
141 and its fractionation during plant uptake, and published date of precipitation Hg (see SI for details). We estimated uncertainty in
142 the mixing model using the variance in precision estimates using Monte Carlo simulations (10,000 trials), with details of the
143 simulation provided in SI (Table S5).

144 2.4 Data Analysis

145 Data were checked for normality (Shapiro–Wilk test) and homogeneity of variance assumptions of statistical tests. The non-
146 normalized data were subjected to a natural logarithmic transformation to ensure a normal distribution. Unpaired Student t-tests
147 were used to assess significant differences between groups (e.g., species), and statistical differences between non-washed and

148 washed aboveground vegetation samples were performed using paired Student t-tests. Linear regression analyses were performed
149 to determine the rate of aboveground biomass Hg uptake over time. Hg mass and turnover rates were calculated by multiplication
150 of Hg concentrations by corresponding biomass or biomass growth and other mass components at the level of sampling plots. All
151 statistical tests were performed with STATA (Version 16.0, Statacorps, College Station, Texas), the mixing model and its
152 uncertainty calculation was performed using Python (Python 3.12.0), and all regressions and statistical tests presented in text,
153 tables, and figures were based on statistical differences with p-values < 0.05. The variability presented in the text and figures is
154 one standard deviation of the means.

155 **3. Results**

156 **3.1 Hg concentrations in aboveground and belowground biomass**

157 Hg concentrations in aboveground tissues showed substantial seasonal variations and species-specific differences, with lowest
158 concentrations in live tissues of *S. alterniflorus* and *D. spicata*, followed by *S. pumilus*, and highest concentrations in *J. gerardii*
159 (Fig 1a). Despite species differences in Hg concentrations, concentrations in bulk vegetation of communities dominated by *S.*
160 *alterniflorus* versus *S. pumilus* (Fig 1b) were not statistically different. This likely occurred because both communities are
161 composed of multiple species. For example, *S. alterniflorus* communities also have a presence of *S. pumilus* plants, while *S. pumilus*
162 communities include large numbers of *D. spicata* plants. Similarly, Hg concentrations of senesced *S. pumilus* and *S. alterniflorus*
163 bulk samples were not statistically significantly different from each other (Fig S1).

164 Hg concentrations in aboveground live biomass strongly increased throughout the growing season between June and November
165 across all species. Figure 2 shows linear increases of Hg concentrations in live aboveground tissues in plots dominated by *S.*
166 *alterniflorus* and *S. pumilus* over time ($r^2 = 0.84$; $p < 0.01$; $n = 50$), with no significant difference in regressions between the two
167 communities. Based on these linear regression slopes, we estimated daily uptake rates of Hg during the growing season of
168 $0.08 \pm 0.01 \mu\text{g kg}^{-1} \text{ day}^{-1}$ for both *Sporobolus* communities. After senescence, Hg concentrations in senesced aboveground biomass
169 measured in spring of the following year (April 2022) were not further enhanced compared to live biomass samples collected in
170 fall (November 2021; $p = 0.19$), (Figs 2 and 4a) suggesting that no statistically significant Hg uptake (or loss) occurred in biomass
171 after senescence.

172 Hg concentrations in live roots and rhizomes (upper 20 cm) were two to three times higher in *S. pumilus* plots ($258.9 \pm 70.3 \mu\text{g kg}^{-1}$
173 1 and $46.6 \pm 14.2 \mu\text{g kg}^{-1}$ respectively) compared to *S. alterniflorus* plots ($84.5 \pm 47.0 \mu\text{g kg}^{-1}$ and $27.9 \pm 1.1 \mu\text{g kg}^{-1}$ respectively) (Fig
174 3, Table S1). In belowground tissues, Hg concentrations were higher in senesced biomass, including dead roots, dead rhizomes,
175 and detritus, compared to live tissues. Belowground tissues also showed higher Hg concentrations than separated soil mineral and
176 humus fractions (although only measured in one *S. pumilus* sample) (Fig 3, Table S1). Bulk soil Hg concentrations (i.e., composed
177 of all fractions listed above) averaged $194.6 \pm 28.3 \mu\text{g kg}^{-1}$ of *S. alterniflorus* community and $171.2 \pm 72.1 \mu\text{g kg}^{-1}$ of *S. pumilus*
178 community in the top 20 cm with no significant difference ($p > 0.05$). Bulk soil Hg concentrations of the 20-40 cm soil in *S.*
179 *alterniflorus* ($279.1 \pm 203.8 \mu\text{g kg}^{-1}$) were almost twice that of *S. pumilus* ($159.1 \pm 122.7 \mu\text{g kg}^{-1}$). Overall, Hg concentrations of live
180 roots ($171.7 \pm 111.9 \mu\text{g kg}^{-1}$) were 11 times higher and live rhizome ($37.3 \pm 13.6 \mu\text{g kg}^{-1}$) were double the concentrations of
181 aboveground live biomass ($16.2 \pm 2.0 \mu\text{g kg}^{-1}$, Table S2).

182 **3.2 Hg pools sizes associated with aboveground and belowground biomass**

183 Aboveground standing live biomass strongly increased from June through August, when it plateaued at a peak biomass in August
184 ($507 \pm 208 \text{ g m}^{-2}$) and September ($498 \pm 118 \text{ g m}^{-2}$, a trend that was consistent among the investigated communities) (Fig 4b). Hg

185 mass contained in live aboveground biomass peaked later (in November) than standing biomass and showed an eight-fold and
186 near-linear increase between June ($0.7 \pm 0.4 \mu\text{g m}^{-2}$) and November ($5.7 \pm 2.1 \mu\text{g m}^{-2}$) (Fig 4c). Peak Hg pools contained in
187 aboveground biomass were $5.7 \pm 2.1 \mu\text{g m}^{-2}$ for live tissue and $3.3 \pm 1.7 \mu\text{g m}^{-2}$ for senesced tissue, for a total combined standing
188 aboveground biomass Hg pools of $9.0 \pm 3.3 \mu\text{g m}^{-2}$ in November (Figs 4c and 5). This number represents our best estimate of total
189 annual Hg assimilation by aboveground vegetation through the year. Standing aboveground biomass (live and senescent) in the
190 spring of the following year (April 2022, $357 \pm 148 \text{ g m}^{-2}$) was 39% lower than total aboveground biomass in November of 2021
191 ($583 \pm 208 \text{ g m}^{-2}$) (Fig 4b) and standing Hg pools were 32% lower in the subsequent spring ($6.1 \pm 1.9 \mu\text{g m}^{-2}$) compared to peak fall
192 levels ($9.0 \pm 3.3 \mu\text{g m}^{-2}$) (Fig 4c), showing substantial losses of standing aboveground biomass and associated Hg pools over winter.
193 Live root biomass in surface soils (top 20 cm) averaged $361 \pm 114 \text{ g m}^{-2}$ and live rhizome biomass were approximately twice as
194 large ($792 \pm 231 \text{ g m}^{-2}$), for a combined live belowground biomass of $1,153 \pm 321 \text{ g m}^{-2}$ (Table S2). Belowground Hg pools associated
195 with these live tissues averaged $70.0 \pm 63.7 \mu\text{g m}^{-2}$ for roots, $38.1 \pm 22.4 \mu\text{g m}^{-2}$ for rhizomes, and $108.1 \pm 83.4 \mu\text{g m}^{-2}$ for the combined
196 live belowground tissue, accounting for less than 0.5% of the total bulk soil Hg pool (Fig 5a, b, Table S2). We observed a much
197 larger Hg pool associated with senesced biomass (roots, rhizomes, and detritus) averaging $4,116 \pm 1,141 \mu\text{g m}^{-2}$, accounting for
198 16.1% of the total bulk soil Hg pool. We estimated a total soil Hg pool in the top 40 cm using measured bulk densities (range of
199 0.22 and 0.37 g cm^{-3}) exceeding $25,000 \mu\text{g m}^{-2}$, with most of this Hg associated with fine soil mineral and humus fraction (83.5%),
200 while much smaller pools were contained in live and senesced plant tissues as mentioned above.

201 3.3 Hg stable isotope signatures to determine Hg sources

202 Live aboveground biomass showed negative mass-dependent fractionation (MDF) values for $\delta^{202}\text{Hg}$ between -1.61% and -1.07% ,
203 and mass-independent (MIF) values were consistently positive with $\Delta^{199}\text{Hg}$ between 0.20% and 0.43% and $\Delta^{200}\text{Hg}$ values between
204 0.04% and 0.11% (Fig 6, Tables S3 and S6). These aboveground isotopic Hg signatures of salt marsh vegetation fell outside of
205 the range commonly reported in foliar samples of terrestrial vegetation, both regarding mass-dependent and mass-independent
206 signatures. Specifically, terrestrial vegetation Hg signatures are substantially more negative in $\delta^{202}\text{Hg}$ values (ranging from -3.06%
207 to -2.37% [inter-quartile range, IQR, $n = 120$]) and both $\Delta^{199}\text{Hg}$ and $\Delta^{200}\text{Hg}$ values in terrestrial vegetation generally show negative
208 values ($\Delta^{199}\text{Hg}$: -0.42% to -0.27% IQR, $\Delta^{200}\text{Hg}$: -0.05% to 0.01% , IQR) (Fig 6, Table S6) (review by Zhou et al., 2021).
209 Stable Hg isotope signatures of salt marsh plant roots were different from aboveground biomass, with less negative values for
210 $\delta^{202}\text{Hg}$ (-0.75% and -0.66%), less positive values for $\Delta^{199}\text{Hg}$ (0.11% and 0.22%), and close to zero values (instead of positive
211 values) for $\Delta^{200}\text{Hg}$ (-0.01% and 0.04%) (Fig 6, Tables S3 and S6). The Hg isotope signatures of roots closely overlapped with
212 signatures in surface marsh soils and deeper marsh soils ($\delta^{202}\text{Hg}$: -0.92% to -0.29% , $\Delta^{199}\text{Hg}$: -0.09% to 0.20% , and $\Delta^{200}\text{Hg}$: $-$
213 0.02% to 0.05% , Tables S3 and S6). Similar to aboveground tissues, salt marsh soil isotopic Hg signatures were largely outside
214 the ranges reported for upland soils, particularly for $\delta^{202}\text{Hg}$ values that are much more negative in upland soils ($\delta^{202}\text{Hg}$ generally
215 between -0.5% and -2.9% ; review by Zhou et al., 2021). Hg isotope signatures of salt marsh rhizomes were highly variable and
216 in-between values observed in foliage and soils. Specifically, rhizomes showed $\delta^{202}\text{Hg}$ values between -1.41% to -0.70% , $\Delta^{199}\text{Hg}$
217 values between 0.13% to 0.22% , and $\Delta^{200}\text{Hg}$ values between -0.05% to 0.04% (Fig 6, Tables S3 and S6).

218 4. Discussion

219 4.1 Salt marsh vegetation and soil Hg concentrations

220 Strong seasonal Hg concentration increases in salt marsh aboveground tissues were consistent with patterns reported from upland
221 ecosystems, such as in forest foliage (Wohlgemuth et al., 2020). In upland systems, foliar Hg increases are attributed in large part

222 to atmospheric GEM uptake, which is taken up during the growing season by stomatal and non-stomatal (i.e., cuticular) leaf uptake
223 (review by Zhou et al., 2021). Hg uptake is controlled by leaf physiological processes and related to photosynthetic capacity, leaf
224 nitrogen concentrations, leaf mass area, and stomatal densities and conductance (Wohlgemuth et al., 2022). In support of a
225 physiologically controlled Hg uptake process in salt marsh plants, we observed that Hg concentrations in senesced biomass in
226 April of 2022 were not significantly enhanced compared to live biomass of the previous November (2021) (Fig 2), indicating that
227 no significant Hg assimilation occurred during wintertime in senesced biomass. However, some increases in Hg concentrations
228 occurred through November even after peak biomass was reached in August and September, which we attribute to continued active
229 plant physiology through late season, as active photosynthesis was measured at least through October at this site (Forbrich et al.,
230 2018; no data is available for November). In contrast to upland plant foliage, however, stable Hg isotope signatures of marsh
231 aboveground biomass show distinctly different Hg source profiles indicating that Hg uptake was not dominated by atmospheric
232 GEM uptake (see below).

233 Estimated daily Hg accumulation rates in *Sporobolus* -dominated aboveground biomass ($0.08 \mu\text{g kg}^{-1} \text{day}^{-1}$, Fig 2) was at the lower
234 range of foliar accumulation rates reported in forest foliage (conifer needle: median of $0.07 \mu\text{g kg}^{-1} \text{day}^{-1}$, deciduous leaf: median
235 of $0.23 \mu\text{g kg}^{-1} \text{day}^{-1}$; Wohlgemuth et al., 2022). This is consistent with the notion that low-statured grassland plants generally
236 exhibit lower Hg concentrations ($5 \mu\text{g kg}^{-1}$ [$1\text{-}31 \mu\text{g kg}^{-1}$]) than trees (e.g., forest foliage ($20 \mu\text{g kg}^{-1}$ [$2\text{-}62 \mu\text{g kg}^{-1}$])) (review by
237 Zhou et al., 2021), although it may also be due to different sources origins of Hg (section 4.2.1 below). Both dominant marsh
238 species in this study also are C4 plants, which previous work shows have lower Hg concentrations compared to C3 species (e.g.,
239 $23 \pm 9 \mu\text{g kg}^{-1}$ versus $53 \pm 12 \mu\text{g kg}^{-1}$, Canário et al., 2017). In a laboratory study with upland plants, suggested reasons for this was
240 catalase activity, which is related to leaf uptake of Hg vapor and is about four times lower in C4 plants than C3 plants (Du and
241 Fang, 1983).

242 Highest Hg concentrations in *S. alterniflorus* and *S. pumilus* were observed in fall ($11.7 \mu\text{g kg}^{-1}$ and $24.0 \mu\text{g kg}^{-1}$, respectively).
243 Hg concentrations fell within concentration ranges reported from other uncontaminated marsh halophytes (Table S8) (Heller and
244 Weber, 1998) (Kraus et al., 1986), but much lower than those from contaminated marshes (up to $90 \mu\text{g kg}^{-1}$; (Windham et al., 2001)
245 (Canário et al., 2017) (Wang et al., 2021).

246 In contrast to upland plants, salt marsh plants (including both *Sporobolus* species) have salt glands which are used for selective
247 and active excretion of sea salt (Kirschner and Zinnert, 2020; Maricle et al., 2009). Salt glands have been linked to excretion of
248 metals (Weis and Weis, 2004), and previous studies reported correlations between leaf surface Hg and sodium (Na) release in *S.*
249 *alterniflorus* suggesting active Hg excretion by salt glands (Weis and Weis, 2004; Windham et al., 2001). Windham et al. (2001)
250 proposed that in the Hackensack Meadowlands, a polluted salt marsh ecosystem, seasonal declines in Hg concentrations in *S.*
251 *alterniflora* leaves between May ($90 \mu\text{g kg}^{-1}$) to July ($30 \mu\text{g kg}^{-1}$) were driven by strong leaf excretion of Hg. By washing leaves of
252 a number of samples, we found that washing removed about 6% of total leaf Hg in *S. alterniflorus* and 16% in *S. pumilus*,
253 respectively (Table S7, note that we use the average wash-off fraction of 11% to estimate throughfall deposition in the mass balance
254 estimation below). The relatively small loss of Hg associated with washing showed that most leaf Hg was structural and likely
255 internal Hg, which along with observed seasonal Hg concentration increases does not support seasonal Hg losses nor seasonal
256 concentration declines that were attributed to salt excretion by Windham et al.

257 Hg concentrations in live roots and rhizomes were much higher (11 and two times, respectively) than aboveground live biomass
258 concentrations. This is consistent with previously reported data that reported high root Hg concentrations in salt marshes (Anjum
259 et al., 2012; Cabrita et al., 2019; Canário et al., 2017; Garcia-Ordiales et al., 2020; Weis and Weis, 2004; Windham et al., 2003).
260 We measured that Hg concentrations were higher in live roots of *S. pumilus* ($258.9 \pm 70.3 \mu\text{g kg}^{-1}$) than in *S. alterniflorus* (84.5 ± 47.0
261 $\mu\text{g kg}^{-1}$) (Fig 3, Table S1). A possible reason for this is finer roots in *S. pumilus* (personal observation), and hence higher surface

262 to volume ratios, which may facilitate soil Hg uptake. In upland ecosystems, fine root Hg concentrations were reported to be higher
263 than in coarse roots as well (Wang et al., 2012; Wang et al., 2020). High root and rhizome Hg concentrations compared to
264 aboveground tissues in marsh plants contrast upland studies that generally report highest concentrations in foliage ($20 \mu\text{g kg}^{-1}$
265 [$2\text{--}62 \mu\text{g kg}^{-1}$]) and much lower concentrations in roots ($7 \mu\text{g kg}^{-1}$ [$2\text{--}70 \mu\text{g kg}^{-1}$]) (Zhou et al., 2021). An exception to this are
266 grassland systems that also report higher root Hg concentrations than in foliage, although the difference was much smaller (e.g.,
267 roots: $41\pm 31 \mu\text{g kg}^{-1}$; leaves: $20\pm 10 \mu\text{g kg}^{-1}$; (Zhou and Obrist, 2021)). Our data also showed generally much lower root Hg
268 concentrations in this marsh compared to contaminated sites (Anjum et al., 2012; Canário et al., 2017; Garcia-Ordiales et al., 2020)
269 (Wang et al., 2021) (Table S8). Overall, published studies suggest a large range of Hg concentrations in belowground salt marsh
270 biomass, which likely is due to different soil Hg concentrations as dominant Hg sources to roots (see section 4.2.1 below). The
271 higher concentrations of root and rhizomes in belowground tissues compared to aboveground biomass also suggests limited
272 translocation between belowground and aboveground tissues (Cavallini et al., 1999; Clemens and Ma, 2016; Graydon et al., 2009;
273 Wang et al., 2012).

274 **4.2 Stable Hg isotope signatures and possible origins of Hg in salt marsh vegetation and soil**

275 **4.2.1 Salt marsh vegetation**

276 One of the largest mass-dependent fractional (MDF) processes in the environmental systems is due to preferential uptake of light
277 atmospheric GEM isotopes by vegetation foliage that leads to large negative $\delta^{202}\text{Hg}$ signatures (generally below -2%), while and
278 mass-independent signatures remain similar to that of atmospheric GEM (Demers et al., 2013; Enrico et al., 2016; Yu et al., 2016),
279 although a recent study also reported inconsistent MIF between foliage and the atmosphere (Wang et al., 2022). In terrestrial
280 ecosystems, studies have shown that the vegetation uptake of atmospheric GEM and subsequent litterfall, throughfall, and plant
281 senescence serves as the primary source of Hg loading (Demers et al., 2013; Jiskra et al., 2015; Louis et al., 2001; Obrist et al.,
282 2017; Wang et al., 2016; Zheng et al., 2016; Zhou et al., 2021). Aboveground tissues of salt marsh plants show a distinctly different
283 signature than upland foliage: specifically, MDF values were much less negative, and values of odd-MIF ($\Delta^{199}\text{Hg}$) and even-MIF
284 ($\Delta^{200}\text{Hg}$) were more positive compared to upland foliage (Fig 6, Table S6).

285 Hg signatures of salt marsh aboveground tissue were close to signatures of salt marsh soils, yet with slightly more negative $\delta^{202}\text{Hg}$
286 values and more positive $\Delta^{199}\text{Hg}$ and $\Delta^{200}\text{Hg}$ values (Table S6). We used a ternary mixing model to identify potential Hg sources
287 and further quantify their contributions for salt marsh plant leaves based on MDF ($\delta^{202}\text{Hg}$) and even-MIF ($\Delta^{200}\text{Hg}$) (Demers et al.,
288 2013; Jiskra et al., 2017, 2021; Obrist et al., 2017). In our model, the dominant three end-member Hg sources include: (1) direct
289 uptake from marsh plant roots as represented by measured stable isotopes of roots, (2) atmospheric GEM uptake with typical
290 upland MDF reported in the literature, implemented using published data of upland foliage isotope data; and (3) precipitation Hg(II)
291 deposition obtained from published literature (see SI for details). Our best estimate shows that the Hg source in salt marsh
292 vegetation consists of a mixture of about 1/3 each from foliar uptake of atmospheric GEM uptake (about 32%), root uptake (about
293 35%), and precipitation deposition (about 33%). Note that these estimates assume that marsh foliage shows the same isotopic GEM
294 fractionation as upland foliage, and further assumes that translocation of root Hg has the same isotope patterns as measured in root
295 biomass. The percentage estimate derived from the tertiary mixing model shows substantial range of uncertainties (Figure S2) due
296 to a low number of samples and errors associated with analytical isotope determination. However, two different Monte Carlo
297 methods to estimate errors both suggest similar source contributions (i.e., about one third from each of the three endmembers).

298 Most notably, the biggest difference of marsh plants compared to upland plants is much less negative $\delta^{202}\text{Hg}$ values, suggesting
299 lower contributions from atmospheric GEM uptake which normally induces strong negative MDF in upland plants. Still, the
300 presence of atmospheric GEM uptake leads to $\delta^{202}\text{Hg}$ values in aboveground tissues that are more negative than in roots and soils.

301 Precipitation, which largely consists of oxidized Hg, shows a typical positive anomaly in $\Delta^{200}\text{Hg}$ linked to upper atmosphere GEM
302 oxidation processes (Enrico et al., 2016; Jiskra et al., 2021; Zhou et al., 2021). Our results also suggest a more important role of
303 root Hg transport to aboveground tissues in salt marsh vegetation (about one third) compared to upland ecosystems which normally
304 reports root origins of less than 5% (review by Zhou et al., 2021). Previous salt marshes suggested inconsistent Hg source patterns:
305 for example, an Hg isotope tracer study suggested minor root-to-leaf transport with soils accounting for a small percentage of Hg
306 in marsh plants (i.e. 2.2-2.7% from Cabrera et al. (2019)), while a study based on bioaccumulation factors suggested a wide and
307 inconstant range of soil Hg contribution to leaves (from 1.7-9.6 % to as high as 46%; Castro et al., 2009).

308 Roots of salt marsh plants show a Hg isotope signature that almost perfectly aligns with the signatures observed in soils, suggesting
309 a dominant soil source. In terrestrial plants, Hg assimilated in belowground biomass also is considered largely of soil origin
310 (Millhollen et al., 2006; Obrist et al., 2018; Zhou et al., 2021). This also has been proposed in aquatic plants (e.g., mangroves,
311 sawgrass) where root Hg largely derives from surrounding soils (Huang et al., 2020; Mao et al., 2013; Yin et al., 2013). Finally,
312 the few measured rhizome Hg isotope signatures indicate a mix of above-ground and belowground Hg sources, although rhizomes
313 show a large variation in isotope signatures with some samples being closer to aboveground tissue and others being closer to root
314 signatures. This observation would be consistent with the role of rhizomes as storage organs with over one year lifetime, whereby
315 carbohydrates and nutrients are re-mobilized between rhizomes and above- and belowground organs based on plant allocation
316 needs.

317 **4.2.2 Salt marsh soil**

318 The salt marsh soil isotope signature fell largely outside the range of soil Hg signatures reported from upland studies. In terrestrial
319 environments, the strong MDF during foliar GEM uptake imprints a similar and typical terrestrial fingerprint on soil Hg, resulting
320 in soil signatures with strong negative $\delta^{202}\text{Hg}$ and $\Delta^{200}\text{Hg}$ values similar to that of vegetation. Mixing models suggest upland soil
321 Hg sources are dominated by atmospheric GEM (accounting for 53% to 92% of the source), which previously originated from
322 plant Hg uptake and subsequent deposition (e.g., plant senescence) of overlying vegetation (Jiskra et al., 2018; Obrist et al., 2018;
323 Zhou et al., 2021; Zhou and Obrist, 2021). These upland soil Hg isotope signatures propagate in watershed runoff (Jiskra, et al.,
324 2017; Woerndle et al., 2018). Soils of our salt marsh study notably lacked the strong $\delta^{202}\text{Hg}$ depletion signal observed in uplands
325 soils (e.g., $\delta^{202}\text{Hg}$ of marsh soils between -0.92‰ and -0.29‰, versus -0.5‰ to -2.5‰ in other soils, review by Zhou et al., 2021).
326 This further supports that sources of Hg in marsh vegetation, which ultimately deposits to soils, are distinctly different from that
327 of upland ecosystems. The isotopic signature of soil samples in Figure 6a also does not support that a simple two-way mixing of
328 plant and precipitation Hg could explain salt marsh soils Hg signatures. Further terrestrial surface runoff, which generally shows
329 typical terrestrial origin signatures (but was not measured in our study), also cannot explain marsh soil Hg isotope patterns.

330 Seawater regularly floods the salt marsh during spring tides and storms and provide sediments for salt marsh soils (Millette et al.,
331 2010). Recently reported ocean water Hg isotopes by Jiskra et al. (2021) show a strong overlap with Hg isotope signatures in salt
332 marsh soil, whereby both $\Delta^{200}\text{Hg}$ and $\delta^{202}\text{Hg}$ fall between the ranges reported for seawater and ocean sediments (Fig S3). However,
333 due to large variability in the data, we are unable to quantify potential source origins using a mixing model. However, the notion
334 of potential ocean Hg sources would be consistent with a sediment mass balance study which showed that sediment loads in the
335 Plum Island Sound estuary were dominated by imported ocean sediments (Hopkinson et al., 2018), with relatively minor import
336 of sediments derived from the watershed. Finally, industrial and legacy contamination sources also may shape salt marsh soil Hg
337 signatures. Generally, industrial Hg isotope signatures have been characterized by large ranges of negative $\delta^{202}\text{Hg}$ values and near-
338 zero to positive $\Delta^{199}\text{Hg}$ and $\Delta^{200}\text{Hg}$ values (Fig S3, Table S6, see SI for details).

339 4.3 Hg mass balance and turnover fluxes associated with biomass dynamics.

340 4.3.1 Aboveground

341 We here estimate a mass balance of Hg sources and sinks associated with aboveground vegetation dynamics and turnover and
342 compare these with previously reported fluxes such as lateral tidal exchanges, published wet and gaseous oxidized Hg, and
343 particulate Hg deposition. Hg inputs to this salt marsh include wet Hg deposition, which based on interpolated data by the NADP
344 program is estimated at $5.2 \mu\text{g m}^{-2} \text{yr}^{-1}$ (NADP, 2017), while a lower estimate of $2.9 \mu\text{g m}^{-2} \text{yr}^{-1}$ has been measured at a nearby
345 coastal site on Cape Cod, Massachusetts (Engle et al., 2010). Combining these two data sets, we estimate a mid-point wet deposition
346 of $4.1 \mu\text{g m}^{-2} \text{yr}^{-1}$. Gaseous oxidized Hg (GOM) and particulate Hg (PHg) deposition in this area was estimated at $1.2 \mu\text{g m}^{-2} \text{yr}^{-1}$
347 based on measurements by Engle et al. (2010) and at $3.0 \mu\text{g m}^{-2} \text{yr}^{-1}$ at a deciduous forest (Harvard Forest) in Massachusetts (Obrist
348 et al., 2021). Hence, a mid-point dry deposition of combined GOM and PHg is estimated at $2.1 \mu\text{g m}^{-2} \text{yr}^{-1}$ (Table 1, Fig 7).
349 Aboveground vegetation Hg dynamics yields a total turnover of $9.0 \pm 3.3 \mu\text{g m}^{-2} \text{yr}^{-1}$ (combined live and senesced biomass at the
350 end of the growing season), and isotope determination suggests that of this, about two thirds (represents an “external source”
351 ($5.9 \pm 2.1 \mu\text{g m}^{-2} \text{yr}^{-1}$) derived from atmospheric GEM and precipitation uptake, while one third is from root uptake ($3.1 \pm 1.1 \mu\text{g m}^{-2}$
352 yr^{-1}) and hence represents an internal plant-soil recycling within the ecosystem. Laboratory sample washing showed that in
353 addition, on average about 11% of foliar Hg concentrations was subject to wash-off. In the absence of field throughfall
354 measurements, we used this fraction to estimate throughfall deposition of Hg of $1.0 \pm 0.4 \mu\text{g m}^{-2} \text{yr}^{-1}$, based on aboveground
355 vegetation Hg pools (noting that this estimate is very preliminary). Combined atmospheric Hg deposition attributable to
356 aboveground vegetation hence is $6.9 \mu\text{g m}^{-2} \text{yr}^{-1}$, and is close to the combined wet, GOM, and PHg deposition of $6.2 \mu\text{g m}^{-2} \text{yr}^{-1}$.
357 Combined atmospheric Hg sources in this system are estimated at $13.1 \mu\text{g m}^{-2} \text{yr}^{-1}$ (Table 1; a range of 7.7 to $19.5 \mu\text{g m}^{-2} \text{yr}^{-1}$).
358 Aboveground vegetation also results in lateral exchange of Hg between marsh and tidal water via wrack export, i.e., losses of
359 plants and surface litter through tidal flushing. Although difficult to measure, wrack export in this area is composed primarily of
360 *S. alterniflorus* plants (Hartman et al., 1983) and has been estimated to constitute 16-19% (mid-point of 17.5%) of accumulated
361 biomass (Duarte, 2017; Duarte and Cebrián, 1996). Hence, we estimate that of the annual Hg uptake by aboveground biomass of
362 $9.0 \pm 3.3 \mu\text{g m}^{-2} \text{yr}^{-1}$, about $1.6 \mu\text{g m}^{-2} \text{yr}^{-1}$ (range of $1.4\text{-}1.7 \mu\text{g Hg m}^{-2} \text{yr}^{-1}$) may be subject to wrack export. Scaling to the whole
363 salt marsh area (40 km^2), the total wrack export from this marsh is estimated around 0.06 kg yr^{-1} (range of $0.06\text{-}0.07 \text{ kg yr}^{-1}$). In a
364 previous study, we quantified Hg exports from the salt marsh system via tidal exchanges of dissolved and particulate Hg (without
365 plants), and estimated $0.7 \mu\text{g m}^{-2} \text{yr}^{-1}$ of dissolved Hg export and $5.6 \mu\text{g m}^{-2} \text{yr}^{-1}$ of particulate Hg export from the marsh to the
366 tidal water (Wang and Obrist, 2022). Our estimated annual Hg export by wrack is higher than lateral export of dissolved Hg, but
367 much smaller than lateral export of particulate Hg. Duarte (2017) and Duarte and Cebrián (1996) estimated that about 27% of NPP
368 is subject to herbivory (e.g., by marsh periwinkle and mummichog), although another study estimated NPP loss due to herbivory
369 at only 5% (Mann, 1988). Hence, an estimated 5% to 27% of plant Hg pools, or $0.5\text{-}2.4 \mu\text{g Hg m}^{-2} \text{yr}^{-1}$, may be subject to herbivory.
370 The largest fraction of NPP (57% to 80%), equivalent to $5.1\text{-}7.2 \mu\text{g Hg m}^{-2} \text{yr}^{-1}$ likely remains in the system and is subject to net
371 accumulation and decomposition. Considering all these inputs and outputs, we estimate a net present-day Hg mass accumulation
372 in this salt marsh ecosystem between $0\text{-}11.5 \mu\text{g m}^{-2} \text{yr}^{-1}$ with a mid-point of $5.2 \mu\text{g m}^{-2} \text{yr}^{-1}$, suggesting that this salt marsh currently
373 represents a small net sink of environmental Hg. Absent of this estimate are gaseous exchange fluxes of GEM between soils/water
374 surfaces and the atmosphere, which are currently being quantified using a tower-based measurement system (Edwards et al., 2005;
375 Obrist et al., 2021).

376 4.3.2 Belowground

377 Many studies show that in salt marsh ecosystems, belowground productivity generally is equal or greater than aboveground
378 biomass production, and this particularly applies for northern marshes (Blum, 1993; Morris, 2007; Tobias and Neubauer, 2019;
379 Windham, 2001). Roots of both dominant species can grow to length of 8 to 20 cm (Blum, 1993; Muench and Elsey-Quirk, 2019).
380 *S. alterniflorus* normally has large and thick rhizomes (normally ranging from 2-4 mm in diameter) with aerenchyma tissues to
381 transport oxygen to submerged belowground tissue for respiration, while *S. pumilus* has relatively dense and fine roots with limited
382 aerenchyma tissue which cannot support aerobic respiration when completely flooded (Muench and Elsey-Quirk, 2019). We
383 measured live root biomass (upper 40 cm) of $444 \pm 87 \text{ g m}^{-2}$ in *S. pumilus* and $278 \pm 61 \text{ g m}^{-2}$ in *S. alterniflorus* cores (Table S1),
384 which is consistent with reported denser root biomass in *S. pumilus* compared to *S. alterniflorus* (Muench and Elsey-Quirk, 2019).
385 Combined live roots and rhizome biomass averaged $1,153 \pm 321 \text{ g m}^{-2}$, and thereby exceeded peak standing aboveground biomass
386 of $830 \pm 415 \text{ g m}^{-2}$ in August 2021.

387 Scaling up Hg pools using these belowground biomass data and measured Hg concentrations yields large belowground Hg pools.
388 For example, the live belowground Hg pool (roots and rhizomes) is $108.1 \pm 83.4 \mu\text{g m}^{-2}$ and more than ten times larger than peak
389 standing aboveground Hg pools ($9.0 \pm 3.3 \mu\text{g m}^{-2}$) (Fig 5a, Table S2). The Hg pool associated with senesced biomass (roots,
390 rhizomes, and detritus) was over an order of magnitude larger ($4,116 \pm 1,141 \mu\text{g m}^{-2}$). Finally, the total pool of Hg in the top 40 cm
391 of these marsh soils (all fractions) are estimated at $>25,000 \mu\text{g m}^{-2}$.

392 Turnover times of salt marsh macrophyte roots have been estimated at 0.6 yr^{-1} (0.2 to 1.9 yr^{-1}) (Ouyang et al., 2017) and 0.5 yr^{-1}
393 (Blum, 1993), although longer turnover times have been proposed for creek-side plants (2.6 yr^{-1} , Blum, 1993). Assuming a
394 belowground biomass turnover rate of 0.6 yr^{-1} (0.2 to 2.6 yr^{-1}), estimated Hg mass turnover associated with belowground biomass
395 (root and rhizome) would be $58.6 \mu\text{g m}^{-2} \text{ yr}^{-1}$ (19.5 to $253.8 \mu\text{g m}^{-2} \text{ yr}^{-1}$) (Table 1, Fig 7). Hence, belowground Hg turnover via
396 plant tissues exceeds that of aboveground tissue ($9.0 \pm 3.3 \mu\text{g m}^{-2} \text{ yr}^{-1}$) by a factor five, although it is largely unclear what the
397 implications of this turnover may be. Given that the source of belowground tissue Hg is largely from soil uptake, large Hg
398 belowground turnover flux does not likely provide an external source and instead represents an internal recycling of Hg between
399 soils and belowground tissues. This recycling of Hg may have been various consequences, such as impacting mobility and
400 bioavailability, phytostabilization by roots (Anjum et al., 2011), or remobilization of Hg associated with root decomposition.

401 The estimated small net sink of environmental Hg in the above Hg mass balance is difficult to reconcile with the presence of very
402 large soil Hg pools exceeding $> 25,000 \mu\text{g m}^{-2}$. It also is not consistent with the notion of this marsh as a hot spot of Hg pollution
403 as reported from high blood Hg levels in predatory birds (Evers et al., 2007; Lane et al., 2020). It is possible that the current sink
404 strength of Hg in this marsh is only a current snapshot in time, and that soil Hg in this marsh Hg largely have derived from historic
405 legacy sources. Such potential sources may include imports of Hg or Hg-contaminated sediments from near-shore ocean into the
406 Plum Island Sound, which in turn possibly may have originated from the nearby Merrimack River, a contaminated watershed from
407 the long industrial history in New England.

408 5. Summary and conclusion

409 Measurements of Hg concentrations, fluxes, and turnover associated with vegetation in a salt marsh ecosystem with high above-
410 and belowground NPP showed an annual Hg uptake in aboveground tissues of $9.0 \pm 3.3 \mu\text{g m}^{-2} \text{ yr}^{-1}$. Using a stable Hg isotope
411 mixing model, we estimate that 35% of aboveground Hg originates from soil Hg uptake, 32% is from atmospheric GEM uptake,
412 and 33% is from precipitation Hg(II) deposition. Estimated annual plant-derived atmospheric Hg deposition from plant senescence
413 (i.e., litterfall) is estimated at $5.9 \pm 2.1 \mu\text{g m}^{-2} \text{ yr}^{-1}$, which is about half of that in forests where plant Hg assimilation of atmospheric

414 GEM is the dominant Hg source. We estimate an additional atmospheric Hg deposition by throughfall of $1.0 \pm 0.4 \mu\text{g m}^{-2} \text{yr}^{-1}$, for
415 combined plant-derived Hg inputs of $6.9 \mu\text{g m}^{-2} \text{yr}^{-1}$. This deposition is similar to combined wet and dry deposition of other
416 atmospheric Hg forms. Seasonal and temporal Hg concentration and mass balance dynamics show strong seasonal increases during
417 active growing season and a lack of concentration changes after senescence over winter, suggesting physiologically controlled
418 uptake pathways. The presence of Hg within the aboveground tissues of salt marshes results in its direct release into tidal waters
419 and oceans through the process of wrack deposition (tidal flushing of vegetation), contributing to an annual export of approximately
420 $1.6 \mu\text{g m}^{-2} \text{yr}^{-1}$. It also leads to herbivory uptake of Hg in a range of 0.5 to $2.4 \mu\text{g Hg m}^{-2} \text{yr}^{-1}$, which may represent an internal
421 recycling within the marsh system or possibly is subject to export (Table 1, Fig 7). The remainder of vegetation Hg is slowly
422 incorporated into soils over winter and during the subsequent year. Overall, we estimate this marsh to presently serve as a small
423 net Hg sink for environmental Hg of $5.2 \mu\text{g m}^{-2} \text{yr}^{-1}$.

424 Belowground Hg pools associated with live tissues ($108.1 \pm 83.4 \mu\text{g m}^{-2}$) were over ten times larger than peak aboveground Hg
425 pools and resulted in a substantial annual Hg turnover flux of $58.6 \mu\text{g m}^{-2} \text{yr}^{-1}$. The source of root Hg is likely from soil uptake,
426 while belowground rhizomes show variable sources both from aboveground and root tissues. Turnover of Hg associated with
427 belowground tissues largely reflects internal recycling between soils and plants, with poorly understood impacts on Hg partitioning,
428 bioavailability, and mobility. Hg associated with roots and rhizomes only accounted for about 0.4% of total belowground Hg pools,
429 with the largest soil Hg pools associated with fine soil mineral and humus fractions (83.5%).

430 **6. Acknowledgements**

431 We thank Keely O’Beirne, Madison Sachs, and Silas Bollen for help with vegetation sampling and laboratory analysis of initial
432 plant and soil mercury samples. We thank Nancy Pau and the Parker River National Wildlife Refuge for sampling permits and
433 acces. We thank Samuel Kelsey, Anne Giblin and other researchers from the Plum Island Ecosystem Long-Term Ecological
434 Research project for support and information about the estuary. Funding was provided by an award from the U.S. National Science
435 Foundation Division of Environmental Biology (Award Number: 2027038).

436 **Code and data availability**

437 Upon request, the original data supporting the conclusions of this study can be provided.

438 **Author contribution**

439 DO and TW designed and carried out the study; TW, BYD, JZ, and JP contributed to samples collection; TW, BYD, JP, PB
440 conducted samples analysis; TW, BYD, IF, EM, PB, and DO contributed to interpreting the data and figures; TW, IF, JZ, ES,
441 BP, CC, and DO contributed to writing and editing the manuscript. All authors contributed to the review of the manuscript. DO
442 and IF secured funding for the project.

443 **Competing interests**

444 The contact author has declared that none of the authors has any competing interests.

445 **Reference**

- 446 Amos, H. M., Jacob, D. J., Kocman, D., Horowitz, H. M., Zhang, Y., Dutkiewicz, S., Horvat, M., Corbitt, E. S., Krabbenhoft, D.
447 P., & Sunderland, E. M. (2014). Global biogeochemical implications of mercury discharges from rivers and sediment
448 burial. *Environmental Science and Technology*, 48(16), 9514–9522. <https://doi.org/10.1021/es502134t>
- 449 Anjum, N. A., Ahmad, I., Válega, M., Pacheco, M., Figueira, E., Duarte, A. C., & Pereira, E. (2011). Impact of seasonal
450 fluctuations on the sediment-mercury, its accumulation and partitioning in *Halimione portulacoides* and *Juncus maritimus*
451 collected from Ria de Aveiro coastal lagoon (Portugal). *Water, Air, and Soil Pollution*, 222(1–4), 1–15.
452 <https://doi.org/10.1007/s11270-011-0799-4>
- 453 Anjum, N. A., Ahmad, I., Válega, M., Pacheco, M., Figueira, E., Duarte, A. C., Pereira, E., Anjum, N. A., Ahmad, I., Válega, :
454 M, Duarte, A. C., Pereira, E., Pacheco, M., & Figueira, E. (2012). Salt marsh macrophyte *Phragmites australis* strategies
455 assessment for its dominance in mercury-contaminated coastal lagoon (Ria de Aveiro, Portugal). *Environ Sci Pollut Res*,
456 19, 2879–2888. <https://doi.org/10.1007/s11356-012-0794-3>
- 457 Arp, W. J., Drake, B. G., Pockman, W. T., Curtis, P. S., & Whigham, D. F. (1993). Manual of the Vascular Flora of the
458 Carolinas. *Vegetatio*, 104(105), 133–143. <https://doi.org/20029742>
- 459 Bertness, M. D. (1991). Zonation of *Spartina patens* and *Spartina alterniflora* in a New England salt marsh. *Ecology*, 72(1), 138–
460 148. <https://doi.org/10.2307/1938909>
- 461 Blum, J. D., & Bergquist, B. A. (2007). Reporting of variations in the natural isotopic composition of mercury. *Analytical and*
462 *Bioanalytical Chemistry*, 388(2), 353–359. <https://doi.org/10.1007/s00216-007-1236-9>
- 463 Blum, J. D., & Johnson, M. W. (2017). Recent developments in mercury stable isotope analysis. *Reviews in Mineralogy and*
464 *Geochemistry*, 82(July 2013), 733–757. <https://doi.org/10.2138/rmg.2017.82.17>
- 465 Blum, L. K. (1993). *Spartina alterniflora* root dynamics in a Virginia marsh. *Marine Ecology Progress Series*, 102, 169–178.
- 466 Cabrita, M. T., Duarte, B., Cesário, R., Mendes, R., Hintelmann, H., Eckey, K., Dimock, B., Caçador, I., & Canário, J. (2019).
467 Mercury mobility and effects in the salt-marsh plant *Halimione portulacoides*: Uptake, transport, and toxicity and tolerance
468 mechanisms. *Science of The Total Environment*, 650, 111–120. <https://doi.org/10.1016/j.scitotenv.2018.08.335>
- 469 Canário, J., Poissant, L., Pilote, M., Caetano, M., Hintelmann, H., & O’Driscoll, N. J. (2017). Salt-marsh plants as potential
470 sources of Hg₀ into the atmosphere. *Atmospheric Environment*, 152, 458–464.
471 <https://doi.org/10.1016/j.atmosenv.2017.01.011>
- 472 Castro, R., Pereira, S., Lima, A., Corticeiro, S., Válega, M., Pereira, E., Duarte, A., & Figueira, E. (2009). Accumulation,
473 distribution and cellular partitioning of mercury in several halophytes of a contaminated salt marsh. *Chemosphere*, 76(10),
474 1348–1355. <https://doi.org/10.1016/j.chemosphere.2009.06.033>
- 475 Cavallini, A., Natali, L., Durante, M., & Maserti, B. (1999). Mercury uptake, distribution and DNA affinity in durum wheat
476 (*Triticum durum* Desf.) plants. *Science of the Total Environment*, 243–244, 119–127. [https://doi.org/10.1016/S0048-](https://doi.org/10.1016/S0048-9697(99)00367-8)
477 [9697\(99\)00367-8](https://doi.org/10.1016/S0048-9697(99)00367-8)
- 478 Cheng, X., Luo, Y., Chen, J., Lin, G., Chen, J., & Li, B. (2006). Short-term C4 plant *Spartina alterniflora* invasions change the
479 soil carbon in C3 plant-dominated tidal wetlands on a growing estuarine Island. *Soil Biology and Biochemistry*, 38(12),
480 3380–3386. <https://doi.org/10.1016/j.soilbio.2006.05.016>
- 481 Clemens, S., & Ma, J. F. (2016). Toxic Heavy Metal and Metalloid Accumulation in Crop Plants and Foods. *Annual Review of*
482 *Plant Biology*, 67, 489–512. <https://doi.org/10.1146/annurev-arplant-043015-112301>
- 483 Curtis, P. S., Balduman, L. M., Drake, B. G., & Whigham, D. F. (1990). Elevated Atmospheric CO₂ Effects on Belowground
484 Processes in C3 and C4 Estuarine Marsh Communities. *Source: Ecology*, 71(5), 2001–2006.

485 Demers, J. D., Blum, J. D., & Zak, D. R. (2013). Mercury isotopes in a forested ecosystem: Implications for air-surface exchange
486 dynamics and the global mercury cycle. *Global Biogeochemical Cycles*, 27(1), 222–238. <https://doi.org/10.1002/gbc.20021>

487 Du, S., & Fang, S. C. (1983). Catalase activity of C3 and C4 species and its relationship to mercury vapor uptake. *Environmental*
488 *and Experimental Botany*, 23(4), 347–353. [https://doi.org/10.1016/0098-8472\(83\)90009-6](https://doi.org/10.1016/0098-8472(83)90009-6)

489 Duarte, C. M. (2017). Reviews and syntheses: Hidden forests, the role of vegetated coastal habitats in the ocean carbon budget.
490 *Biogeosciences*, 14(2), 301–310. <https://doi.org/10.5194/bg-14-301-2017>

491 Duarte, C. M., & Cebrián, J. (1996). The fate of marine autotrophic production. *Limnology and Oceanography*, 41(8), 1758–
492 1766. <https://doi.org/10.4319/LO.1996.41.8.1758>

493 Edwards, G. C., Rasmussen, P. E., Schroeder, W. H., Wallace, D. M., Halfpenny-Mitchell, L., Dias, G. M., Kemp, R. J., &
494 Ausma, S. (2005). Development and evaluation of a sampling system to determine gaseous Mercury fluxes using an
495 aerodynamic micrometeorological gradient method. *Journal of Geophysical Research D: Atmospheres*, 110(10), 1–11.
496 <https://doi.org/10.1029/2004JD005187>

497 Elsey-Quirk, T., Seliskar, D. M., & Gallagher, J. L. (2011). Nitrogen Pools of Macrophyte Species in a Coastal Lagoon Salt
498 Marsh: Implications for Seasonal Storage and Dispersal. *Estuaries and Coasts*, 34(3), 470–482.
499 <https://doi.org/10.1007/s12237-011-9379-5>

500 Engle, M. A., Tate, M. T., Krabbenhoft, D. P., Schauer, J. J., Kolker, A., Shanley, J. B., & Bothner, M. H. (2010). Comparison of
501 atmospheric mercury speciation and deposition at nine sites across central and eastern North America. *Journal of*
502 *Geophysical Research Atmospheres*, 115(18). <https://doi.org/10.1029/2010JD014064>

503 Enrico, M., Balcom, P., Johnston, D. T., Foriel, J., & Sunderland, E. M. (2021). Simultaneous combustion preparation for
504 mercury isotope analysis and detection of total mercury using a direct mercury analyzer. *Analytica Chimica Acta*, 1154.
505 <https://doi.org/10.1016/j.aca.2021.338327>

506 Enrico, M., Roux, G. Le, Maruszczak, N., Heimbürger, L. E., Claustres, A., Fu, X., Sun, R., & Sonke, J. E. (2016). Atmospheric
507 Mercury Transfer to Peat Bogs Dominated by Gaseous Elemental Mercury Dry Deposition. *Environmental Science and*
508 *Technology*, 50(5), 2405–2412. <https://doi.org/10.1021/acs.est.5b06058>

509 Evers, D. C., Han, Y.-J., Driscoll, C. T., Kamman, N. C., Goodale, M. W., Lambert, K. F., Holsen, T. M., Chen, C. Y., Clair, T.
510 A., & Butler, T. (2007). Biological Mercury Hotspots in the Northeastern United States and Southeastern Canada.
511 *BioScience*, 57(1), 29–43. <https://doi.org/10.1641/b570107>

512 Fisher, L. S., & Wolfe, M. H. (2012). Examination of mercury inputs by throughfall and litterfall in the Great Smoky Mountains
513 National Park. *Atmospheric Environment*, 47, 554–559. <https://doi.org/10.1016/j.atmosenv.2011.10.017>

514 Forbrich, I., Giblin, A. E., & Hopkinson, C. S. (2018). Constraining Marsh Carbon Budgets Using Long-Term C Burial and
515 Contemporary Atmospheric CO2 Fluxes. *Journal of Geophysical Research: Biogeosciences*, 123(3), 867–878.
516 <https://doi.org/10.1002/2017JG004336>

517 Fu, X., Zhang, H., Liu, C., Zhang, H., Lin, C. J., & Feng, X. (2019). Significant Seasonal Variations in Isotopic Composition of
518 Atmospheric Total Gaseous Mercury at Forest Sites in China Caused by Vegetation and Mercury Sources. *Environmental*
519 *Science and Technology*, 53(23), 13748–13756. <https://doi.org/10.1021/acs.est.9b05016>

520 Garcia-Ordiales, E., Roqueñí, N., & Loredó, J. (2020). Mercury bioaccumulation by *Juncus maritimus* grown in a Hg
521 contaminated salt marsh (northern Spain). *Marine Chemistry*, 226, 103859.
522 <https://doi.org/10.1016/j.marchem.2020.103859>

523 Graydon, J. A., St. Louis, V. L., Hintelmann, H., Lindberg, S. E., Sandilands, K. A., Rudd, J. W. M., Kelly, C. A., Tate, M. T.,
524 Krabbenhoft, D. P., & Lehnher, I. (2009). Investigation of uptake and retention of atmospheric Hg(II) by boreal forest

525 plants using stable Hg isotopes. *Environmental Science and Technology*, 43(13), 4960–4966.
 526 <https://doi.org/10.1021/es900357s>

527 Grigal, D. F. (2003). Mercury Sequestration in Forests and Peatlands. *Journal of Environmental Quality*, 32(2), 393–405.
 528 <https://doi.org/10.2134/jeq2003.3930>

529 Grigal, D. F., Kolka, R. K., Fleck, J. A., & Nater, E. A. (2000). Mercury budget of an upland-peatland watershed.
 530 *Biogeochemistry*, 50(1), 95–109. <https://doi.org/10.1023/A:1006322705566>

531 Hartman, J., Caswell, H., & Valiela, I. (1983). Effects of wrack accumulation on salt marsh vegetation. *Oceanologica Acta*,
 532 *Actes 17e*(February), 99–102.

533 He, L., Chen, J. M., Pan, Y., Birdsey, R., & Kattge, J. (2012). Relationships between net primary productivity and forest stand
 534 age in U.S. forests. *Global Biogeochemical Cycles*, 26(3). <https://doi.org/10.1029/2010GB003942>

535 Heller, A. A., & Weber, J. H. (1998). Seasonal study of speciation of mercury(II) and monomethylmercury in *Spartina*
 536 *alterniflora* from the Great Bay Estuary, NH. *Science of the Total Environment*, 221(2–3), 181–188.
 537 [https://doi.org/10.1016/S0048-9697\(98\)00285-X](https://doi.org/10.1016/S0048-9697(98)00285-X)

538 Hopkinson, C. S., Morris, J. T., Fagherazzi, S., Wollheim, W. M., & Raymond, P. A. (2018). Lateral Marsh Edge Erosion as a
 539 Source of Sediments for Vertical Marsh Accretion. *Journal of Geophysical Research: Biogeosciences*, 123(8), 2444–2465.
 540 <https://doi.org/10.1029/2017JG004358>

541 Huang, S., Jiang, R., Song, Q., Zhang, Y., Huang, Q., Su, B., Chen, Y., Huo, Y., & Lin, H. (2020). Study of mercury transport
 542 and transformation in mangrove forests using stable mercury isotopes. *Science of the Total Environment*, 704, 135928.
 543 <https://doi.org/10.1016/j.scitotenv.2019.135928>

544 Iverfeldt, Å. (1991). Mercury in forest canopy throughfall water and its relation to atmospheric deposition. *Water Air & Soil*
 545 *Pollution*, 56(1), 553–564. <https://doi.org/10.1007/BF00342299>

546 Jackson, A. K., Evers, D. C., Etterson, M. A., Condon, A. M., Folsom, S. B., Detweiler, J., Schmerfeld, J., & Cristol, D. A.
 547 (2011). Mercury Exposure Affects The Reproductive Success of a Free-living Terrestrial Songbird, the Carolina Wren
 548 (*Thryothorus Ludovicianus*). In *The Auk* (Vol. 128, Issue 4). <https://doi.org/10.1525/auk.2011.11106>

549 Jiskra, M., Heimbürger-Boavida, L.-E., Desgranges, M.-M., Petrova, M. V., Dufour, A., Ferreira-Araujo, B., Masbou, J.,
 550 Chmeleff, J., Thyssen, M., Point, D., & Sonke, J. E. (2021). Mercury stable isotopes constrain atmospheric sources to the
 551 ocean. *Nature*, 597(7878), 678–682. <https://doi.org/10.1038/s41586-021-03859-8>

552 Jiskra, M., Sonke, J. E., Obrist, D., Bieser, J., Ebinghaus, R., Myhre, C. L., Pfaffhuber, K. A., Wängberg, I., Kyllönen, K.,
 553 Worthy, D., Martin, L. G., Labuschagne, C., Mkololo, T., Ramonet, M., Magand, O., & Dommergue, A. (2018). A
 554 vegetation control on seasonal variations in global atmospheric mercury concentrations. *Nature Geoscience*, 11(4), 244–
 555 250. <https://doi.org/10.1038/s41561-018-0078-8>

556 Jiskra, M., Wiederhold, J. G., Skyllberg, U., Kronberg, R. M., Hajdas, I., & Kretzschmar, R. (2015). Mercury Deposition and
 557 Re-emission Pathways in Boreal Forest Soils Investigated with Hg Isotope Signatures. *Environmental Science and*
 558 *Technology*, 49(12), 7188–7196. <https://doi.org/10.1021/acs.est.5b00742>

559 Jiskra, M., Wiederhold, J. G., Skyllberg, U., Kronberg, R. M., & Kretzschmar, R. (2017). Source tracing of natural organic
 560 matter bound mercury in boreal forest runoff with mercury stable isotopes. *Environmental Science: Processes and Impacts*,
 561 19(10), 1235–1248. <https://doi.org/10.1039/c7em00245a>

562 Kirschner, A. S., & Zinnert, J. C. (2020). Two low-lying coastal grassland species differ in mechanistic response to saline
 563 flooding stress. *Plant Ecology*, 221(6), 475–485. <https://doi.org/10.1007/s11258-020-01026-z>

564 Kraus, M. L., Weis, P., & Crow, J. H. (1986). The excretion of heavy metals by the salt marsh cord grass, *Spartina alterniflora*,

565 and *Spartina*'s role in mercury cycling. *Marine Environmental Research*, 20(4), 307–316. <https://doi.org/10.1016/0141->
566 1136(86)90056-5

567 Lane, O., Adams, E. M., Pau, N., O'Brien, K. M., Regan, K., Farina, M., Schneider-Moran, T., & Zarudsky, J. (2020). Long-
568 term monitoring of mercury in adult saltmarsh sparrows breeding in Maine, Massachusetts and New York, USA 2000–
569 2017. In *Ecotoxicology* (Vol. 29, Issue 8). Springer US. <https://doi.org/10.1007/s10646-020-02180-w>

570 Lane, O. P., O'Brien, K. M., Evers, D. C., Hodgman, T. P., Major, A., Pau, N., Ducey, M. J., Taylor, R., & Perry, D.
571 (2011). Mercury in breeding saltmarsh sparrows (*Ammodramus caudacutus caudacutus*). *Ecotoxicology*, 20(8), 1984–
572 1991. <https://doi.org/10.1007/s10646-011-0740-z>

573 Liu, M., Zhang, Q., Maavara, T., Liu, S., Wang, X., & Raymond, P. A. (2021). Rivers as the largest source of mercury to coastal
574 oceans worldwide. *Nature Geoscience*, 14(9), 672–677. <https://doi.org/10.1038/s41561-021-00793-2>

575 Louis, V. L. S. T., Rudd, J. W. M., Kelly, C. A., Hall, B. D., Rolffhus, K. R., Scott, K. J., Lindberg, S. E., & Dong, W. (2001).
576 Importance of the forest canopy to fluxes of methyl mercury and total mercury to boreal ecosystems. *Environmental*
577 *Science and Technology*, 35(15), 3089–3098. <https://doi.org/10.1021/es001924p>

578 Mann, K. H. (1988). Production and use of detritus in various freshwater, estuarine, and coastal marine ecosystems. *Limnology*
579 *and Oceanography*, 33(4part2), 910–930. <https://doi.org/10.4319/LO.1988.33.4PART2.0910>

580 Mao, Y., Li, Y., Richards, J., & Cai, Y. (2013). Investigating uptake and translocation of mercury species by sawgrass (*Cladium*
581 *jamaicense*) using a stable isotope tracer technique. *Environmental Science and Technology*, 47(17), 9678–9684.
582 <https://doi.org/10.1021/es400546s>

583 Maricle, B. R., Koteyeva, N. K., Voznesenskaya, E. V., Thomasson, J. R., & Edwards, G. E. (2009). Diversity in leaf anatomy,
584 and stomatal distribution and conductance, between salt marsh and freshwater species in the C4 genus *Spartina* (Poaceae).
585 *New Phytologist*, 184(1), 216–233. <https://doi.org/10.1111/J.1469-8137.2009.02903.X>

586 Marques, B., Lillebø, A. I., Pereira, E., & Duarte, A. C. (2011). Mercury cycling and sequestration in salt marshes sediments: An
587 ecosystem service provided by *Juncus maritimus* and *Scirpus maritimus*. *Environmental Pollution*, 159(7), 1869–1876.
588 <https://doi.org/10.1016/j.envpol.2011.03.036>

589 Millette, T. L., Argow, B. A., Marciano, E., Hayward, C., Hopkinson, C. S., & Valentine, V. (2010). Salt Marsh
590 Geomorphological Analyses via Integration of Multitemporal Multispectral Remote Sensing with LIDAR and GIS .
591 *Journal of Coastal Research*, 265, 809–816. <https://doi.org/10.2112/jcoastres-d-09-00101.1>

592 Millhollen, A. G., Gustin, M. S., & Obrist, D. (2006). Foliar Mercury Accumulation and Exchange for Three Tree Species.
593 *Environmental Science & Technology*, 40(19), 6001–6006. <https://doi.org/10.1021/es0609194>

594 Morris, J. T. (2007). Estimating Net Primary Production of Salt Marsh Macrophytes. In *Principles and Standards for Measuring*
595 *Primary Production* (Vol. 15, Issue 1, pp. 106–119). Oxford University Press.
596 <https://doi.org/10.1093/acprof:oso/9780195168662.003.0007>

597 Morris, J. T., Sundberg, K., & Hopkinson, C. S. (2013). Salt marsh primary production and its responses to relative sea level and
598 nutrients in estuaries at Plum Island, Massachusetts, and North Inlet, South Carolina, USA. *Oceanography*, 26(3), 78–84.
599 <https://doi.org/10.5670/oceanog.2013.48>

600 Muench, A., & Elsey-Quirk, T. (2019). Competitive reversal between plant species is driven by species-specific tolerance to
601 flooding stress and nutrient acquisition during early marsh succession. *J Appl Ecol*, 56, 2236–2247.
602 <https://doi.org/10.1111/1365-2664.13458>

603 NADP. (2017). *National Atmospheric Deposition Program, Mercury Deposition Network*.
604 http://nadp.slh.wisc.edu/maplib/pdf/mdn/hg_Conc_2017.pdf

605 Niu, Z., Zhang, X., Wang, Z., & Ci, Z. (2011). Field controlled experiments of mercury accumulation in crops from air and soil.
606 *Environmental Pollution*, 159(10), 2684–2689. <https://doi.org/10.1016/j.envpol.2011.05.029>

607 NOAA. (2020). *National Oceanic and Atmospheric Administration Tide Predictions*.
608 <https://www.tidesandcurrents.noaa.gov/noaatidepredictions.html?id=8441241>

609 Obrist, D., Agnan, Y., Jiskra, M., Olson, C. L., Colegrove, D. P., Hueber, J., Moore, C. W., Sonke, J. E., & Helmig, D. (2017).
610 Tundra uptake of atmospheric elemental mercury drives Arctic mercury pollution. *Nature*, 547(7662), 201–204.
611 <https://doi.org/10.1038/nature22997>

612 Obrist, D., Kirk, J. L., Zhang, L., Sunderland, E. M., Jiskra, M., & Selin, N. E. (2018). A review of global environmental
613 mercury processes in response to human and natural perturbations: Changes of emissions, climate, and land use. *Ambio*,
614 47(2), 116–140. <https://doi.org/10.1007/s13280-017-1004-9>

615 Obrist, D., Roy, E. M., Harrison, J. L., Kwong, C. F., William Munger, J., Moosmüller, H., Romero, C. D., Sun, S., Zhou, J., &
616 Commane, R. (2021). Previously unaccounted atmospheric mercury deposition in a midlatitude deciduous forest.
617 *Proceedings of the National Academy of Sciences of the United States of America*, 118(29).
618 <https://doi.org/10.1073/pnas.2105477118>

619 Ouyang, X., Lee, S. Y., & Connolly, R. M. (2017). The role of root decomposition in global mangrove and saltmarsh carbon
620 budgets. In *Earth-Science Reviews* (Vol. 166, pp. 53–63). <https://doi.org/10.1016/j.earscirev.2017.01.004>

621 Raymond, P. A., & Hopkinson, C. S. (2003). Ecosystem Modulation of Dissolved Carbon Age in a Temperate Marsh-Dominated
622 Estuary. *Ecosystems*, 6(7), 694–705. <https://doi.org/10.1007/s10021-002-0213-6>

623 Rea, A. W., Keeler, G. J., & Scherbatskoy, T. (1996). The deposition of mercury in throughfall and litterfall in the Lake
624 Champlain watershed: A short-term study. *Atmospheric Environment*, 30(19), 3257–3263. [https://doi.org/10.1016/1352-2310\(96\)00087-8](https://doi.org/10.1016/1352-2310(96)00087-8)

625

626 Sun, L., Shao, D., Xie, T., Gao, W., Ma, X., Ning, Z., & Cui, B. (2020). How does *Spartina alterniflora* invade in salt marsh in
627 relation to tidal channel networks? Patterns and processes. *Remote Sensing*, 12(18). <https://doi.org/10.3390/RS12182983>

628 Tobias, C., & Neubauer, S. (2009). Salt Marsh Biogeochemistry - An Overview. In G. M. E. Perillo, E. Wolanski, D. R. Cahoon,
629 & M. M. Brinson (Eds.), *Coastal Wetlands: An Integrated Ecosystem Approach* (pp. 1–57). Elsevier.

630 Tobias, Craig, & Neubauer, S. C. (2019). Salt Marsh Biogeochemistry—An Overview. *Coastal Wetlands: An Integrated*
631 *Ecosystem Approach*, 539–596. <https://doi.org/10.1016/B978-0-444-63893-9.00016-2>

632 U.S. EPA. (1998). Method 7473, Mercury in solids and solutions by thermal decomposition, amalgamation, and atomic
633 absorption spectrophotometry. In *Revision 0. Washington, DC*.

634 Valiela, I., Teal, J. M., & Persson, N. Y. (1976). Production and dynamics of experimentally enriched salt marsh vegetation:
635 Belowground biomass. *Limnology and Oceanography*, 21(2), 245–252. <https://doi.org/10.4319/lo.1976.21.2.0245>

636 Visser, J. M., Midway, S., Baltz, D. M., & Sasser, C. E. (2018). Ecosystem structure of tidal saline marshes. In *Coastal*
637 *Wetlands: An Integrated Ecosystem Approach* (pp. 519–538). Elsevier. <https://doi.org/10.1016/B978-0-444-63893-9.00015-0>

638

639 Wang, J. J., Guo, Y. Y., Guo, D. L., Yin, S. L., Kong, D. L., Liu, Y. S., & Zeng, H. (2012). Fine root mercury heterogeneity:
640 Metabolism of lower-order roots as an effective route for mercury removal. *Environmental Science and Technology*, 46(2),
641 769–777. <https://doi.org/10.1021/es2018708>

642 Wang, T., & Obrist, D. (2022). Inorganic and methylated mercury dynamics in estuarine water of a salt marsh in Massachusetts,
643 USA. *Environmental Pollution*, 294. <https://doi.org/10.1016/j.envpol.2021.118657>

644 Wang, X., Bao, Z., Lin, C. J., Yuan, W., & Feng, X. (2016). Assessment of Global Mercury Deposition through Litterfall.

645 *Environmental Science and Technology*, 50(16), 8548–8557. <https://doi.org/10.1021/acs.est.5b06351>

646 Wang, X., Yuan, W., Lin, C.-J., & Feng, X. (2022). Mercury cycling and isotopic fractionation in global forests. *Critical*
647 *Reviews in Environmental Science and Technology*, 52(21), 3763–3786. <https://doi.org/10.1080/10643389.2021.1961505>

648 Wang, X., Yuan, W., Lin, C.-J., Zhang, L., Zhang, H., & Feng, X. (2019). Climate and Vegetation As Primary Drivers for Global
649 Mercury Storage in Surface Soil. *Environmental Science & Technology*, 53(18), 10665–10675.
650 <https://doi.org/10.1021/acs.est.9b02386>

651 Wang, X., Yuan, W., Lin, C. J., Luo, J., Wang, F., Feng, X., Fu, X., & Liu, C. (2020). Underestimated Sink of Atmospheric
652 Mercury in a Deglaciated Forest Chronosequence. *Environmental Science and Technology*, 54(13), 8083–8093.
653 <https://doi.org/10.1021/acs.est.0c01667>

654 Wang, X., Yuan, W., Lin, C. J., Wang, D., Luo, J., Xia, J., Zhang, W., Wang, F., & Feng, X. (2022). Root uptake dominates
655 mercury accumulation in permafrost plants of Qinghai-Tibet Plateau. *Communications Earth and Environment*, 3(1), 1–10.
656 <https://doi.org/10.1038/s43247-022-00619-y>

657 Wang, Y., Wang, Z., Zheng, X., & Zhou, L. (2021). Influence of *Spartina alterniflora* invasion on mercury storage and
658 methylation in the sediments of Yangtze River estuarine wetlands. *Estuarine, Coastal and Shelf Science*, 265(June 2021),
659 107717. <https://doi.org/10.1016/j.ecss.2021.107717>

660 Weis, J. S., & Weis, P. (2004). Metal uptake, transport and release by wetland plants: implications for phytoremediation and
661 restoration. *Environment International*, 30(5), 685–700. <https://doi.org/10.1016/j.envint.2003.11.002>

662 Wilson, C. A., Hughes, Z. J., FitzGerald, D. M., Hopkinson, C. S., Valentine, V., & Kolker, A. S. (2014). Saltmarsh pool and
663 tidal creek morphodynamics: Dynamic equilibrium of northern latitude saltmarshes? *Geomorphology*, 213, 99–115.
664 <https://doi.org/10.1016/j.geomorph.2014.01.002>

665 Windham, L, Weis, J. ., & Weis, P. (2003). Uptake and distribution of metals in two dominant salt marsh macrophytes, *Spartina*
666 *alterniflora* (cordgrass) and *Phragmites australis* (common reed). *Estuarine, Coastal and Shelf Science*, 56(1), 63–72.
667 [https://doi.org/10.1016/S0272-7714\(02\)00121-X](https://doi.org/10.1016/S0272-7714(02)00121-X)

668 Windham, Lisamarie. (2001). Comparison of biomass production and decomposition between *Phragmites australis* (common
669 reed) and *spartina patens* (salt hay grass) in brackish tidal marshes of New Jersey, USA. *Wetlands*, 21(2), 179–188.
670 [https://doi.org/10.1672/0277-5212\(2001\)021\[0179:COBPAD\]2.0.CO;2](https://doi.org/10.1672/0277-5212(2001)021[0179:COBPAD]2.0.CO;2)

671 Windham, Lisamarie, Wei, J. S., & Weis, P. (2001). *Patterns and Processes of Mercury Release from Leaves of Two Dominant*
672 *Salt Marsh Macrophytes , Phragmites australis and Spartina alterniflora*. 24(6), 787–795.
673 <https://doi.org/https://doi.org/10.2307/1353170>

674 Windham, Lisamarie, Weis, J. S., & Weis, P. (2001). Patterns and processes of mercury release from leaves of two dominant salt
675 marsh macrophytes, *Phragmites australis* and *Spartina alterniflora*. *Estuaries*, 24(6 A), 787–795.
676 <https://doi.org/10.2307/1353170>

677 Windham, Lisamarie, Weis, J. S., Weis, P., Wei, J. S., Weis, P., Weis, J. S., & Weis, P. (2001). Patterns and Processes of
678 Mercury Release from Leaves of Two Dominant Salt Marsh Macrophytes , *Phragmites australis* and *Spartina alterniflora*.
679 *Estuaries*, 24(6), 787–795. <https://doi.org/https://doi.org/10.2307/1353170>

680 Woerndle, G. E., Tsz-Ki Tsui, M., Sebestyen, S. D., Blum, J. D., Nie, X., & Kolka, R. K. (2018). New Insights on Ecosystem
681 Mercury Cycling Revealed by Stable Isotopes of Mercury in Water Flowing from a Headwater Peatland Catchment.
682 *Environmental Science and Technology*, 52(4), 1854–1861. <https://doi.org/10.1021/acs.est.7b04449>

683 Wohlgemuth, L., Osterwalder, S., Joseph, C., Kahmen, A., Hoch, G., Alewell, C., & Jiskra, M. (2020). A bottom-up
684 quantification of foliar mercury uptake fluxes across Europe. *Biogeosciences*, 17(24), 6441–6456.

685 <https://doi.org/10.5194/bg-17-6441-2020>

- 686 Wohlgemuth, L., Rautio, P., Ahrends, B., Russ, A., Vesterdal, L., Waldner, P., Timmermann, V., Eickenscheidt, N., Fürst, A.,
687 Greve, M., Roskams, P., Thimonier, A., Nicolas, M., Kowalska, A., Ingerslev, M., Merilä, P., Benham, S., Iacoban, C.,
688 Hoch, G., ... Jiskra, M. (2022). Physiological and climate controls on foliar mercury uptake by European tree species.
689 *Biogeosciences*, 19, 1335–1353. <https://doi.org/10.5194/bg-19-1335-2022>
- 690 Wolanski, E., Perillo, G. M. E., Brinson, M. M., & Cahoon, D. R. (2009). *Coastal Wetlands: A Synthesis*. Elsevier. Amsterdam,
691 Países Bajos. <http://www.elsevier.com>
- 692 Yin, R., Feng, X., & Meng, B. (2013). Stable mercury isotope variation in rice plants (*Oryza sativa* L.) from the Wanshan
693 mercury Mining District, SW China. *Environmental Science and Technology*, 47(5), 2238–2245.
694 <https://doi.org/10.1021/es304302a>
- 695 Yu, B., Fu, X., Yin, R., Zhang, H., Wang, X., Lin, C. J., Wu, C., Zhang, Y., He, N., Fu, P., Wang, Z., Shang, L., Sommar, J.,
696 Sonke, J. E., Maurice, L., Guinot, B., & Feng, X. (2016). Isotopic composition of atmospheric mercury in China: New
697 evidence for sources and transformation processes in air and in vegetation. *Environmental Science and Technology*, 50(17),
698 9362–9369. <https://doi.org/10.1021/acs.est.6b01782>
- 699 Zhang, Y., Jacob, D. J., Dutkiewicz, S., Amos, H. M., Long, M. S., & Sunderland, E. M. (2015). Biogeochemical drivers of the
700 fate of riverine mercury discharged to the global and Arctic oceans. *Global Biogeochemical Cycles*, 29(6), 854–864.
701 <https://doi.org/10.1002/2015GB005124>
- 702 Zheng, W., Obrist, D., Weis, D., & Bergquist, B. A. (2016). Mercury isotope compositions across North American forests.
703 *Global Biogeochemical Cycles*, 30(10), 1475–1492. <https://doi.org/10.1002/2015GB005323>
- 704 Zhou, J., & Obrist, D. (2021). Global Mercury Assimilation by Vegetation. *Environmental Science and Technology*, 55(20),
705 14245–14257. <https://doi.org/10.1021/acs.est.1c03530>
- 706 Zhou, J., Obrist, D., Dastoor, A., Jiskra, M., & Ryjkov, A. (2021). Vegetation uptake of mercury and impacts on global cycling.
707 *Nature Reviews Earth & Environment*, 2(4), 269–284. <https://doi.org/10.1038/s43017-021-00146-y>
- 708
- 709

710 **Figures and tables**

711

712

713

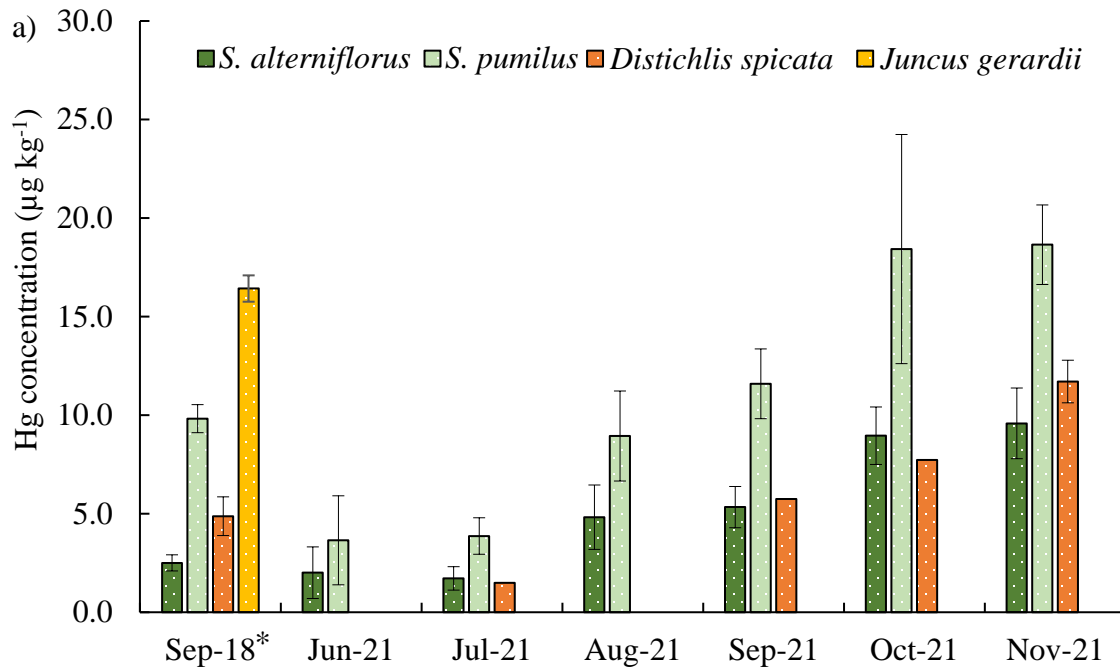
714

715

716

717

718



719

720

721

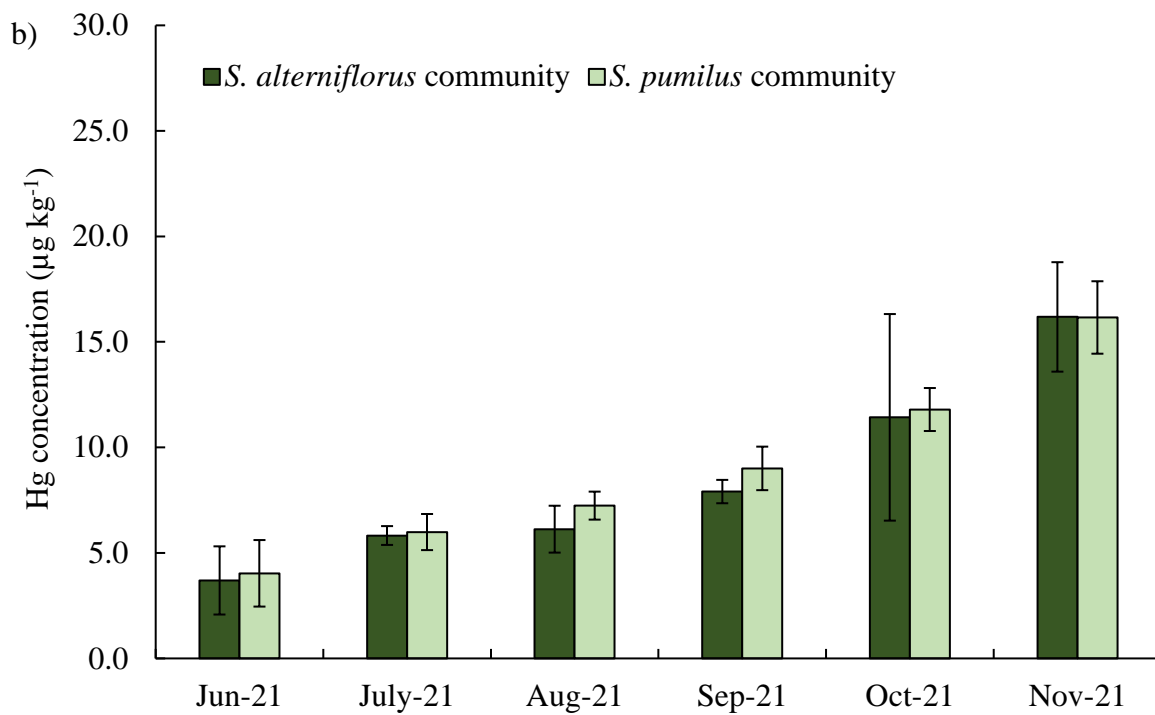
722

723

724

725

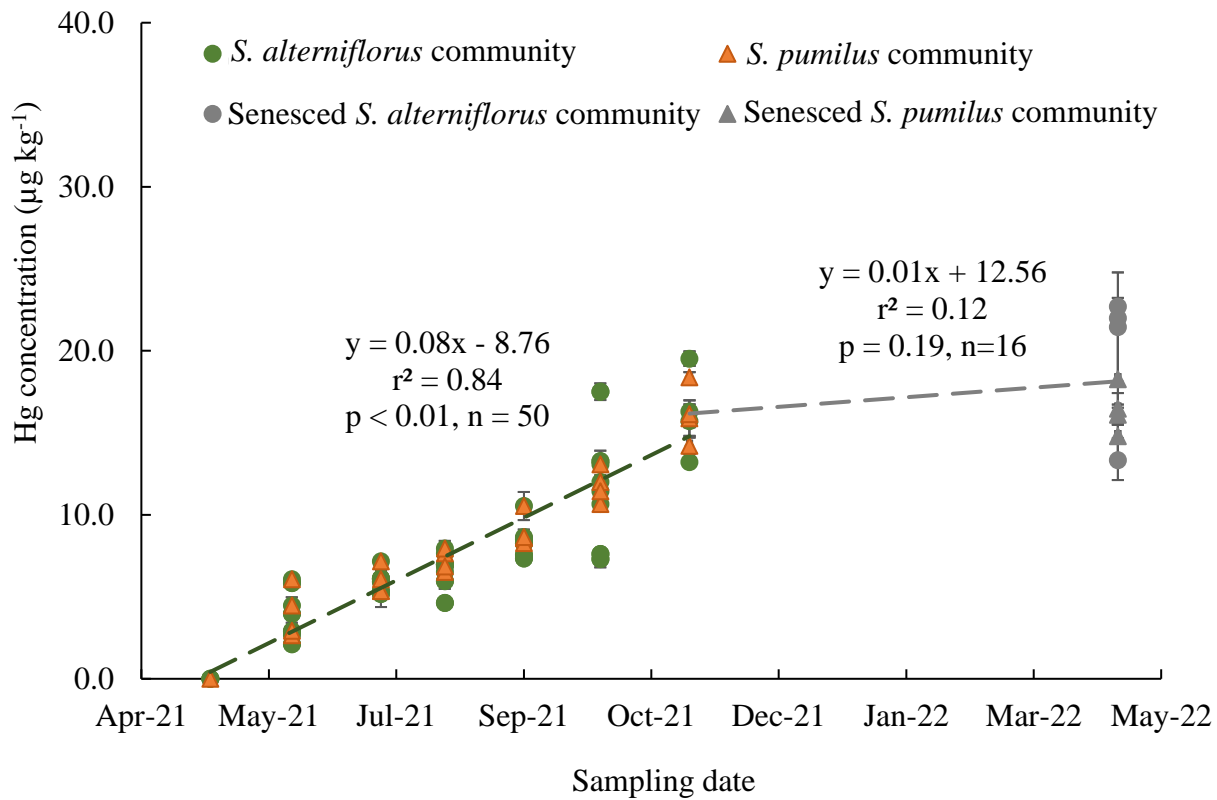
726



727

728

729 **Figure 1. Seasonal Hg concentrations of the four dominated salt marsh live plant species in 2018 and 2021 a), and seasonal Hg**
 730 **concentrations of the *S. alterniflorus* and *S. pumilus* communities in 2021 b). Different colors indicate different plant species. Standard**
errors indicate four replicates. *: Standard errors indicate duplicates for a sample.

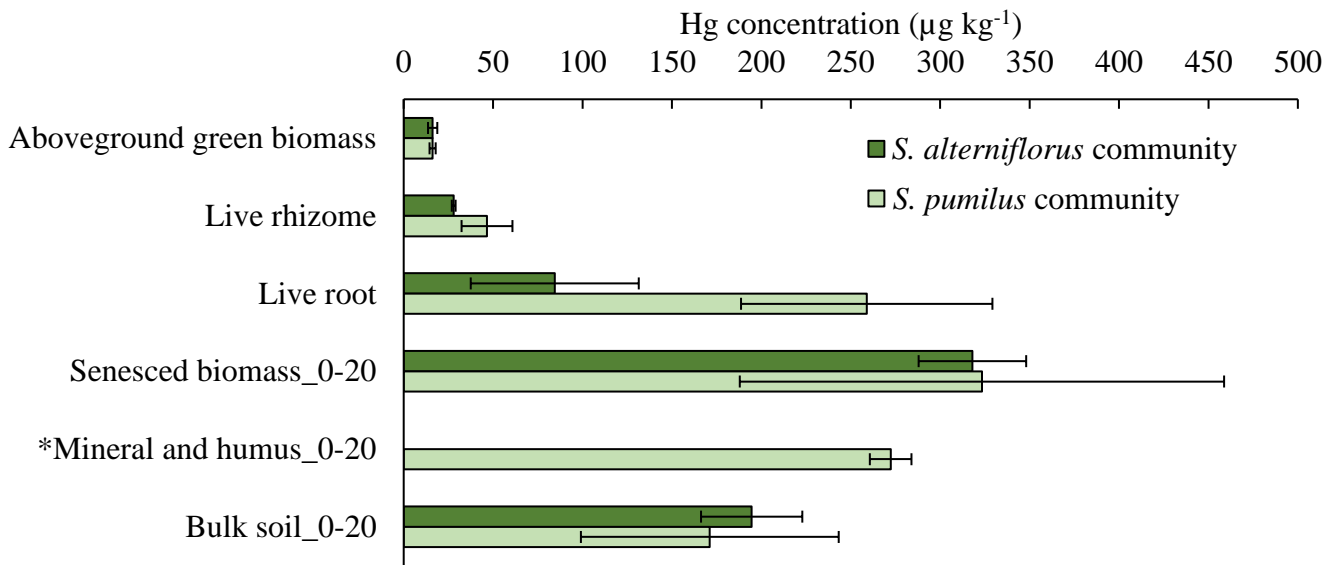


731

732 **Figure 2.** Hg concentrations of live and senesced aboveground biomass of *S. alterniflorus* and *S. pumilus* communities corresponds with
 733 sampling dates in 2021. Green circles indicate live *S. alterniflorus* communities, orange triangles indicate live *S. pumilus* communities,
 734 grey circles indicate senesced *S. alterniflorus* communities, and grey triangles indicate senesced *S. pumilus* communities. Standard errors
 735 indicate four replicates. Note that data in April 2021 was extrapolated and set to zero based on phenological observations that showed
 736 no presence of live biomass at this time.

737

738



739

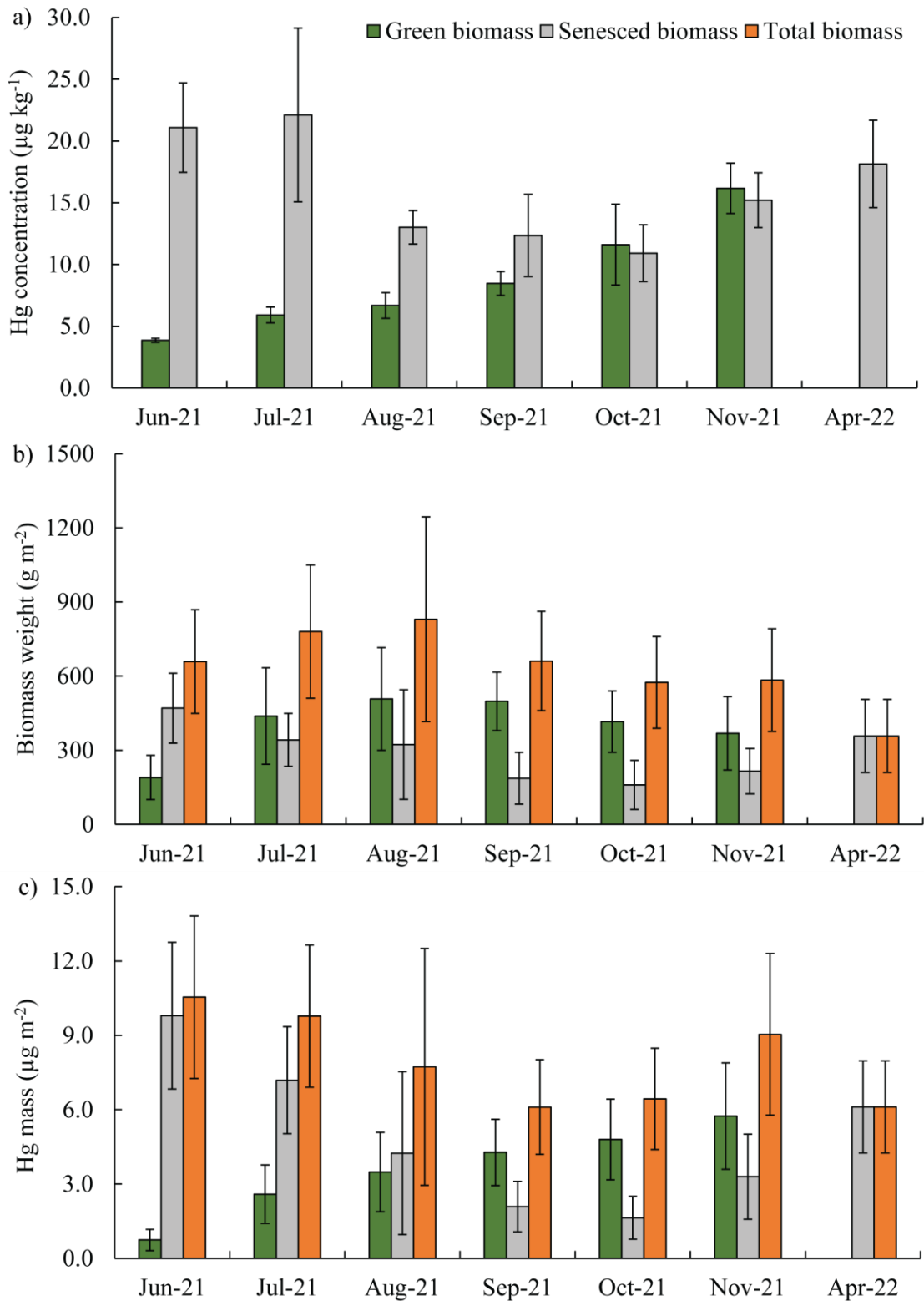
740

741

742

743

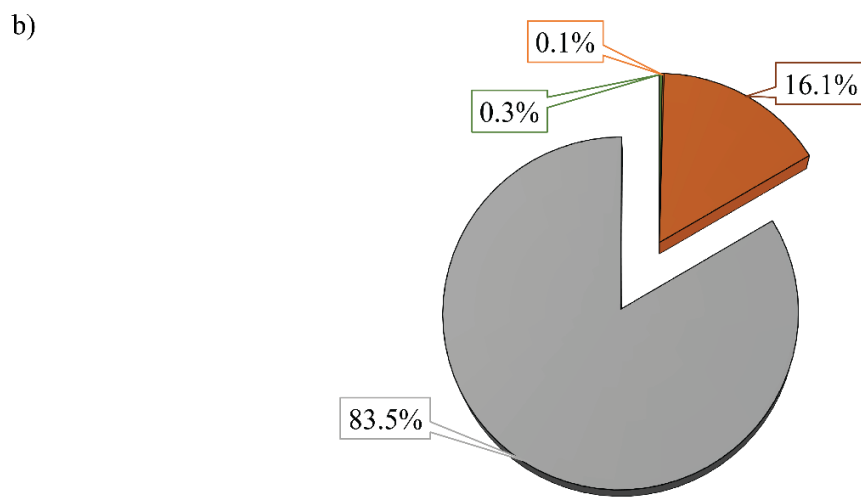
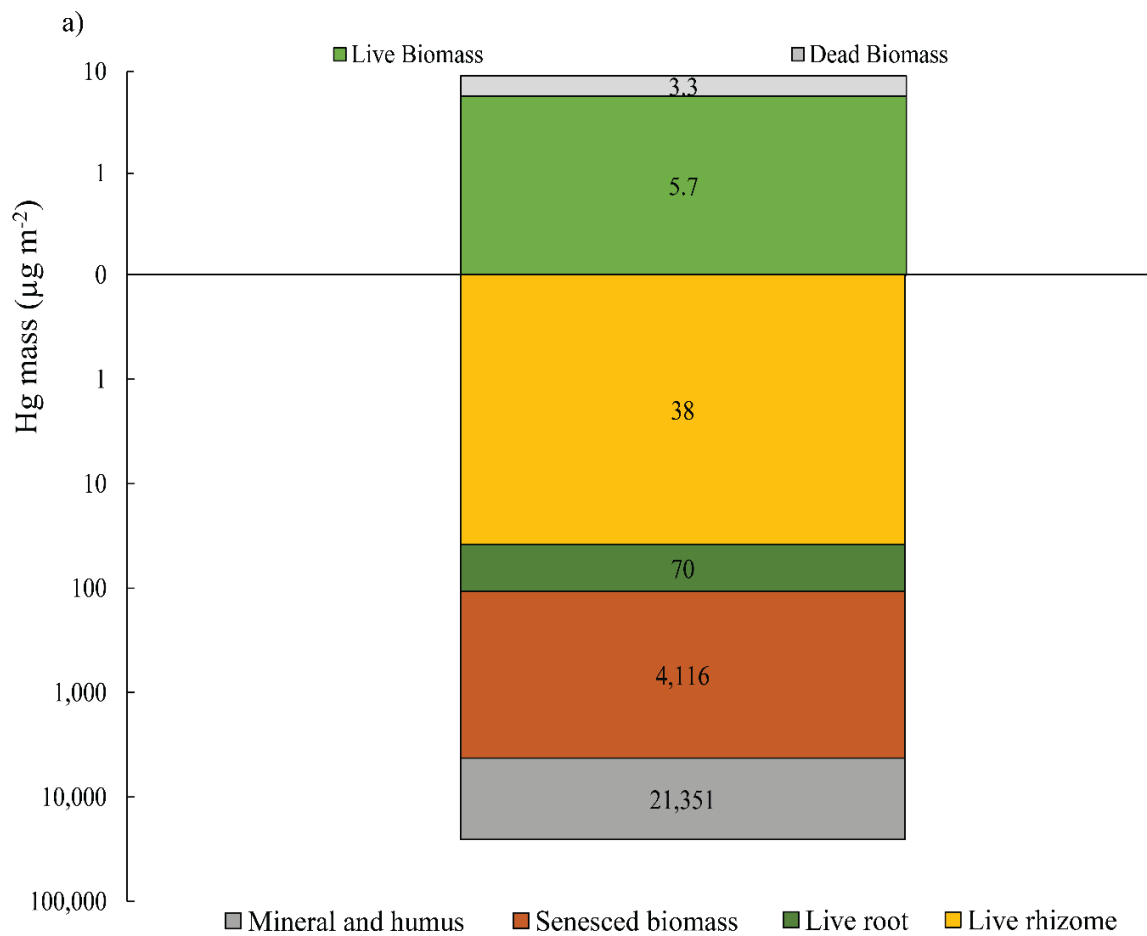
Figure 3. Hg concentrations in live above- and belowground biomass of *S. alterniflorus* and *S. pumilus* communities, as well as Hg concentrations of minerals and humus and bulk soils up to depth of 20cm covered by these two plant species. Dark green columns denote *S. alterniflorus* community, light green columns denote *S. pumilus* community. Standard errors indicate multiple sample analysis. *Hg concentration in mineral and humus only present one site covered by *S. pumilus*, and standard errors are duplicates.



745

746 **Figure 4** Seasonal patterns of Hg concentrations a), biomass dry weight b), and Hg mass c) in aboveground live and senesced biomass
 747 from June 2021 to April 2022. The green columns represent live biomass, grey columns represent senesced biomass, and orange columns
 748 represent total biomass weight and Hg mass of adding live and senesced biomass. Standard errors indicate four replicates. *: no live
 749 biomass was visible in April 2022 so that senesced biomass equals total biomass

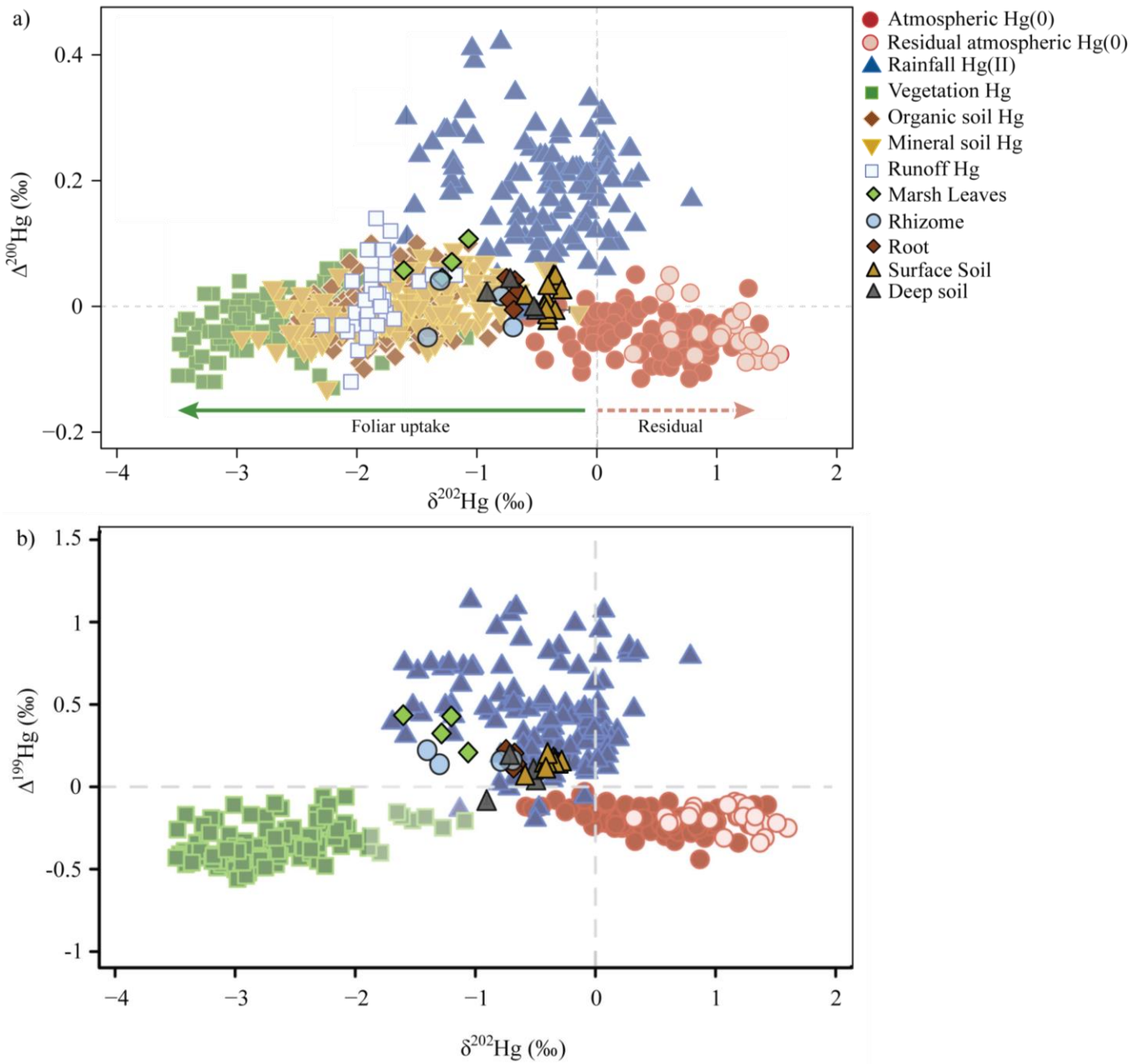
750



751

752 **Figure 5. Hg mass of above- and belowground biomass, including live and senesced biomass, and mineral and humus fractions in a soil**
 753 **depth of 40cm, a), and percentages of Hg mass contribution from belowground sections to the Hg soil pool of a soil depth of 40cm, b).**
 754 **Different colors indicate of different sections of the marsh.**

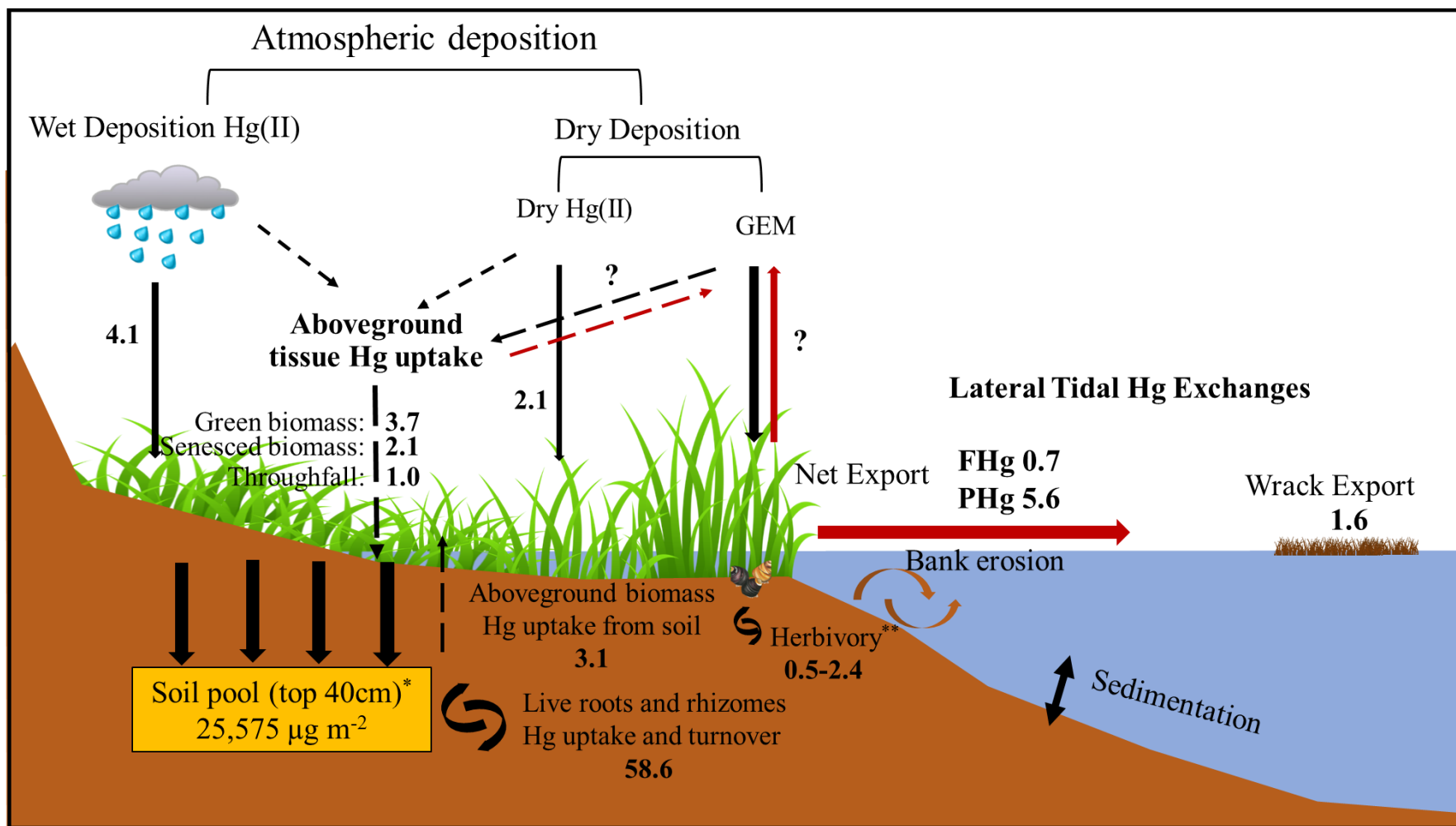
755



757

758 **Figure 6. Hg isotopes in salt marsh plants and soils, and foliage a) of $\Delta^{200}\text{Hg}$ and $\delta^{202}\text{Hg}$, and b) of $\Delta^{199}\text{Hg}$ and $\delta^{202}\text{Hg}$. Composition of**
 759 **Hg sources in marsh vegetation and soils (surface and deep soil layers), and all previously published currently available isotope data of**
 760 **sources of Hg in vegetation and in terrestrial sinks, atmospheric Hg(0) and Hg(II) sources (Zhou et al., 2021), plotted as a) even-mass-**
 761 **independent ($\Delta^{200}\text{Hg}$) versus mass- dependent ($\delta^{202}\text{Hg}$) isotopes a) and b) odd-mass-independent ($\Delta^{199}\text{Hg}$) versus mass- dependent**
 762 **($\delta^{202}\text{Hg}$) isotopes.**

763



765

766 Figure 7. Hg mass balance of the study salt marsh ecosystem. The values shown mostly represent the median Hg flux values with unit of $\mu\text{g m}^{-2} \text{yr}^{-1}$, except for the soil pool*, which
 767 represents an averaged value, and herbivory**, which indicates a range. The red arrows indicate the emission of Hg back to the atmosphere and its export out of the salt marsh. The
 768 dashed arrows represent Hg fluxes related to aboveground biomass

Table 1 Hg mass balance of the study salt marsh ecosystem.

Category	Item	Hg flux ($\mu\text{g m}^{-2} \text{ yr}^{-1}$)	Percent of Hg sources	Reference	Hg fluxes scaled to the marsh (kg yr^{-1})*	
Present-day Hg Mass Balance (total inputs minus exports)	Deposition	Green aboveground biomass	3.7±1.4 (1.3-5.0)	65% atmospheric Hg	This study	0.15 (0.05-0.20)
		Senesced aboveground biomass	2.1±1.1 (1.2-4.7)	65% atmospheric Hg	This study	0.08 (0.05-0.19)
		Total aboveground biomass	5.9±2.1 (3.1-9.7)	65% atmospheric Hg	This study	0.24(0.12-0.39)
		Throughfall	1.0±0.4 (0.5-1.6)	100% atmospheric Hg	This study	0.04(0.02-0.06)
		Wet Hg(II)	4.1 (2.9-5.2)	100% atmospheric Hg	(Engle et al. 2010, NADP, 2017)	0.16 (0.12- 0.21)
		Dry Hg(II)	2.1 (1.2-3.0)	100% atmospheric Hg	(Engle et al., 2010, Obrist et al., 2021)	0.08 (0.05-0.12)
	Total		13.1 (7.7-19.5)		This study	0.52 (0.31-0.78)
	Export	Tidal export dissolved Hg	0.7	100% marsh soil Hg	Wang and Obrist, 2022	0.03
		Tidal export particulate Hg	5.6	100% marsh soil Hg	Wang and Obrist, 2023	0.22
		Wrack	1.6 (1.4-1.7)	100% marsh plants	This study	0.06 (0.06-0.07)
	Total		7.9 (7.7 - 8.0)		This study	0.32 (0.31-0.32)
	Net mass accumulation (estimated total deposition – total export)		5.2 (0-11.5)		This study	0.21 (0.0-0.46)
	Internal Cycling	Green aboveground biomass	1.9±0.7 (0.7-2.6)	35% soil Hg	This study	0.08 (0.03-0.10)
Senesced aboveground biomass		1.1±0.6 (0.6-2.5)	35% soil Hg	This study	0.04 (0.02-0.10)	
Total aboveground biomass		3.1±1.1 (1.6-5.1)	35% soil Hg	This study	0.12 (0.06-0.20)	
Roots and rhizomes		58.6 (19.5-253.8)	90% soil Hg	This study	2.3 (0.8-10.2)	
Herbivory		0.5-2.4	100% marsh plants	This study		
Total Soil Hg Mass	Item	Hg mass ($\mu\text{g m}^{-2}$)	Percent of Hg sources	Reference	Hg mass scaled to the marsh (kg)*	
	Soil Hg mass top 40 cm	25,575±14,409 (16,127-46,997)		This study	1,023±576 (645-1880)	

770 * Salt marsh area (vegetated): 40 km²

